A Physics-Based Approach to Modeling Grassland Fires

William Mell[A], Mary Ann Jenkins[B], Jim Gould[C,D], Phil Cheney[C]

[A]Building and Fire Research Laboratory, National Institute of Standards and Technology, Gaithersburg, MD USA
[B]Department of Earth & Space Science & Engineering, York University, Toronto, ON M3J 1P3, Canada
[C]Ensis-Forest Biosecurity and Protection, CSIRO, Kingston, ACT,Australia
[D]Bushfire Cooperative Research Centre, East Melbourne, Victoria, Australia

January 19, 2007

Abstract

Physics-based coupled fire-atmosphere models are based on approximations to the governing equations of fluid dynamics, combustion, and the thermal degradation of solid fuel. They require significantly more computational resources than the most commonly used fire spread models, which are semi-empirical or empirical. However, there are a number of fire behavior problems, of increasing relevance, that are outside the scope of empirical and semi-empirical models. Examples are wildland-urban interface fires, assessing how well fuel treatments work to reduce the intensity of wildland fires, and investigating the mechanisms and conditions underlying blow-up fires and fire spread through heterogeneous fuels. These problems are not amenable to repeatable full scale field studies. Suitably validated coupled atmosphere-fire models are one way to address these problems. This paper describes the development of a three-dimensional, fully-transient, physics based, computer simulation approach for modelling fire spread through surface fuels. Grassland fires were simulated and compared to findings from Australian experiments. Predictions of the head fire spread rate for a range of ambient wind speeds and ignition line-fire lengths compared favorably to experiments. In addition, two specific experimental cases were simulated in order to evaluate how well the model predicts the development of the entire fire perimeter.

Running head: Physics-based grassland fire model
Extra keywords: Computational Fluid Dynamics (CFD), fire spread, wildland fire, numerical simulation

To appear *International Journal of Wildland Fire*

Corresponding author:
William Mell
Building and Fire Research Laboratory, National Institute of Standards and Technology
100 Bureau Drive, Stop 8663, Gaithersburg, MD 20899-8663 USA
ruddy@nist.gov; (201)975-4797; (301)975-4052 (fax)

1 Introduction and Background

Wildfires and wildland-urban interface (WUI) fires are driven by complex physical and chemical processes, operating on vastly different scales, whose interactions depend on coupling between the atmosphere, topography, fire, and solid fuels. Both wildland and WUI fires are very difficult, if not impossible, to study with full-scale repeatable experiments in the field due to their expense, safety implications, and variations in atmosphere, terrain, and fuel conditions. Yet, there has been a long standing need to improve our understanding of these fires (Williams 1982). Forests are strongly connected to the wildfire regime, and their nature is dependent on the frequency, extent, and severity of forest fires. Reconciling the need to protect forest lands that are valuable for industry and recreation with the natural role of fire in maintaining forest ecosystems is a priority in developing fire management in Canada. Both fire occurrence and average annual area burned by Canadian forest fires have increased over the past three decades. The records indicate 6,000 fires per year in the 1930 to 1960 period to almost 10,000 fires per year during the 1980s and 1990 (Murphy et al. 2000), where the change in fire occurrence is attributed to a growing population, expanded forest use, and an increased detection capability (Stock and Simard 1993).

Studies in the United States (Appicello 2006) suggest that as a consequence of the past wildfire management practice of total suppression, many of America's forests have accumulations of historic dense, dead fallen vegetation. It is maintained that this, along with (and possibly dominated by) climate change in the western U.S. (Westerling et al. 2006) has made forests more dangerous from a fire safety perspective and weakened ecologically; fires ignite more quickly, burn with greater intensity, and spread more rapidly than in the past. According to the US General Accountability Office, in the 1990s the number and size of wildfires, and the associated fire fighting cost, has increased dramatically (GAO 1999). In the United States forest fires are an increasing threat to lives and property. The number of homes at risk of fire in the wildland-urban interface (WUI) are also likely to increase due to the growing number of people moving into fire-prone areas (GAO 2005). Based on 2000 census information 36% of homes in the United States are within the WUI (Stewart et al. 2003). In California alone, homes in the WUI account for 42% of the total homes. Wildland fires in Southern California spreading through WUI areas in 2003 resulted in $2 billion of estimated insured losses (GAO 2005). Homes at risk to WUI fires are also located in Arizona, Colorado, Georgia, New Mexico, New York and Florida (Zicherman 2004).

The most commonly used operational models for wildland fire spread rely on empirically derived relations to predict the spread rate of a fire and quantities derived from the spread rate. Examples of such models are BehavePlus (Andrews et al. 2003) and FARSITE (Finney 1998) in the United States, the Forest Service Fire Behavior Prediction System (Hirsch 1996) in Canada, and the Mk 4 MacArthur Fire Danger Meters (Nobel et al. 1980), and the CSIRO Grassland Fire Spread Meter in Australia. The essence of these models is that the local fire spread rate is prescribed as a function of wind speed, terrain slope, humidity, and fuel characteristics. No account is taken, except for tuning the coefficients, for the fire/fuel and fire/atmosphere interactions. The data used to derive the empirical correlations employed in these models were taken either directly from field experiments/observations (Hirsch 1996; Nobel et al. 1980) or from laboratory scale experiments with a flat flame front with a quasi-steady spread rate across spatially homogeneous surface fuels on flat beds without a wind (Rothermel 1972; Albini 1976). Spread rates used in BehavePlus and FARSITE are based on semi-empirical relations developed by Rothermel (1972). Such models provide fire spread predictions quickly and can be easily applied to conditions that are outside those in the laboratory, sometimes with non-physical results (Beer 1991). They are also unable to predict fire behavior in the intermix of vegetative and structural fuels that comprise the wildland-urban interface.

As discussed by Finney (1998) FARSITE is unable to predict the transient behavior of a fire due to changes in the local environment induced by the fire itself (e.g., fire/atmosphere interaction). This is because the fire shape, size and spread rate are assumed constant for a given fuel, wind, and slope. The prediction of local wind and the interaction of the fire and wind is of major importance to predicting fire behavior, especially severe, fire behavior Albini (1993). Fires where strong fire-atmosphere interactions occur, such as crown fires, routinely strain the credibility of the empirical fire spread models.

Development of these models began in the 1970s. At that time computational resources and numerical methods were not sufficiently advanced to allow three-dimensional time dependent simulations of wildland fires. With the dramatic increase in the capability of computers and numerical approaches in the last 30 years, population growth in wildland-urban interface areas, and the increased role of prescribed burns in forest management, there is an opportunity and a need for more capable physics-based fire models. Suitably validated physics-based models for wildland and WUI fires, which predict both fire spread and smoke transport, have a number of applications:

- evaluate operational models over a wide range of relevant conditions,
- provide more realistic sources of heat and smoke for the new generation of regional smoke transport models operating on present day computational platforms (e.g., BlueSky (2004)),
- help land and smoke managers plan and evaluate prescribed burns,
- assess the effects of fire on vegetation during prescribed burns,
- assess how fuel treatments influence fire spread and the resulting fire effects on vegetation,
- provide a means by which established communities or homeowners can assess and/or reduce their risk to WUI fires,
- help plan firewise communities by both reducing the risk from fire spread and planning smoke free evacuation routes,
- deliver predictions of fire spread and smoke transport to incident managers to aid their management of fire fighting and evacuation logistics.

In general, simulations of wildfires require models for both the fire/fuel interaction and the fire/atmosphere interaction. The fire/fuel interaction involves gas generation by solid fuel pyrolysis, the subsequent combustion of the fuel gases, and the resulting heat flux back to the solid fuel, driving continued pyrolysis and fire spread. The fire/atmosphere interaction involves the response of both the fire and its plume to the ambient winds, and the response of the atmosphere to the buoyant fire plume. The fire/atmosphere interaction can alter the orientation and geometry of the fire plume, influencing the distribution and intensity of the net heat flux to the solid fuel, and the downwind transport of firebrands and smoke. At larger spatial and temporal scales, the interaction of the fire plume with the atmosphere can result in macroscopic (on the scale of the fire front) atmospheric processes such as pyrocumulus formation. At even larger scales, diurnal cycles in humidity and temperature, and synoptic weather patterns, can influence the behavior of the fire and its smoke plume.

Figure 1 is a schematic showing the atmosphere, fire, and vegetative fuel components of wildland fire models at the corners of a triangle. Different fire models are located on the figure according to the emphasis they place on each of these three components and their interaction. The Canadian FBPS (Hirsch 1996), the Australian McArthur meters (Nobel et al. 1980), and the US FARSITE (Finney 1998) and BEHAVE (Andrews 1986; Andrews et al. 2003) are all located in region V since these empirical or semi-empirical, not physics-based, fire models and they require only inputs describing the vegetative fuel, terrain, and wind.

The focus of this paper is on modeling solid fuel pyrolysis, heat transfer, gas phase combustion

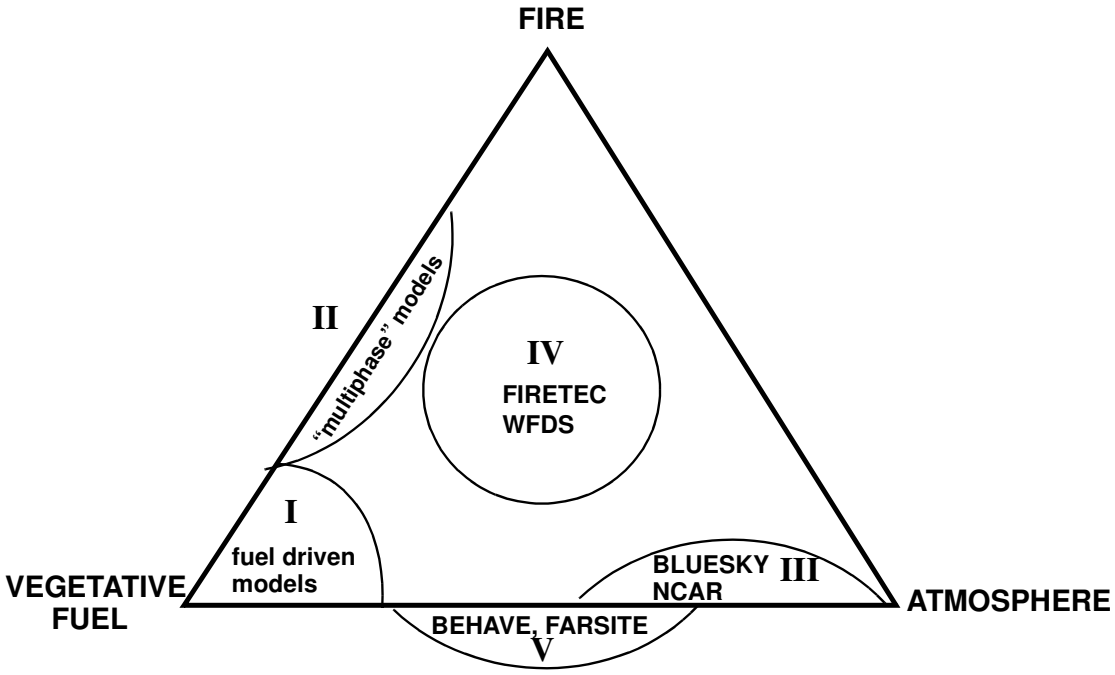

Figure 1: A schematic showing the relationship of different wildland fire models. Each approach is located according to its emphasis on the atmosphere, vegetative fuel, and/or fire component(s) of the working model. See text for a discussion of the figure.

(i.e., the fire/fuel interaction) and local fire/atmosphere interaction. A fuller investigation of large-scale fire/atmosphere interactions described above, along with firebrand generation and transport, will be considered later. In this paper the overall modeling approach is broken into two components: 1) the pyrolysis of vegetative fuels and, 2) gas phase combustion. Models for each are implemented within the Fire Dynamics Simulator (FDS) developed at the Building and Fire Research Laboratory at the National Institute of Standards and Technology (NIST) (McGrattan 2005) over the last 30 years. FDS numerically solves a form of the Navier-Stokes equations appropriate for low-speed, thermally-driven flow with an emphasis on smoke and heat transport from fires. It is aimed at solving practical fire protection engineering problems (i.e., fires in structures) while providing a tool to study fundamental fire dynamics and combustion. Simulations can be run on single or multiple processors on most modern computer platforms. The version of FDS used here is extended to include fire spread in vegetative fuels and is referred to as WFDS (WUI Fire Dynamics Simulator).

In this paper the development of the current version of WFDS is described and evaluated by comparing its predictions of fire behavior to open grassland fire experiments conducted by CSIRO in Australia (Cheney et al. 1993; Cheney and Gould 1995). The relatively simple scenario of grassland surface fires provides an appropriate first step to evaluating WFDS since the fuels are to a good approximation thermally thin, spatially homogeneous, occur on flat terrain, and fire spread is mostly restricted to horizontal directions (i.e., there is relatively little upward fire spread as can occur in suspended vegetation such as large tree crowns).

2 Review of physics-based wildland fire models

Fire models can be classified into three types (Pastor et al. 2003): empirical, semi-empirical, or theoretical. Empirical models involve no physics-based modeling since they are derived from statistical correlations of a given experimental data set. Semi-empirical models are based on energy conservation but do not distinguish between the different modes of heat transfer (conductive, convective, radiative). Theoretical models attempt to solve (in some approximation) the equations governing fluid dynamics, combustion, and heat transfer. Here we refer to theoretical models as physics-based models since the physical processes governing the hydrodynamics, combustion, and energy transfer are modeled. Vegetative fuels and fires in a wildland setting are categorized as ground, surface, or crown types (e.g., Chap. 4 in Johnson and Miayanishi (2001)). Examples of fuels in surface fires include fallen twigs, leaves, bark, branches, grasses, and shrubs less than 1.8 m tall (Davis 1959).

As discussed in the previous section, a complete physics-based wildland fire simulation would include models of the fire/atmosphere and the fire/fuel interactions. In this section a short overview of existing physics-based models that can be applied to surface fires is given. Figure 1 is used to order the discussion. Note that some approaches are formulated to include a wide range of physics but then implemented in a simpler, reduced, form. This is true of the approach formulated by Sero-Guillaume and Margeri (2002), and then implemented by Margeri and Sero-Guillaume (2002). Such cases are placed on Fig. 1 based on the version of the model that was implemented.

Over the last 60 years, starting with Fons (1946), many physics-based fire/fuel models for a fire spreading along a spatially homogeneous fuel bed have been presented. Examples are Albini (1985); De Mestre et al. (1989); Margeri and Sero-Guillaume (2002). Weber (1991) provides an excellent review of these (and other) models up to circa 1989. In these approaches the fire/atmosphere interaction is not modeled. Relevant flame properties, such as the temperature and flame geometry, and therefore the heat flux from the fire, are fixed. This removes the need for modeling the fire in the fire/fuel interaction. While these models have slope and wind inputs, their physical modeling is focused on heat transfer within the fuel. For this reason they are designated 'fuel driven' models on Fig. 1 and located in Region I where modeling of the fire and atmosphere physics is less emphasized. The basis of most of these models is that the steady flame spread rate is determined by how long it takes the solid fuel ahead of the flame to reach an ignition temperature at an idealized two-dimensional ignition interface. Such models are useful for exploring the relative contributions of the different modes of heat transfer but only for conditions appropriate for steady flame spread where net wind speed and direction, fuel properties, terrain, etc., are all constant.

More recently, multidimensional, transient, wildfire simulation approaches that use the methods of computational fluid dynamics to include the fire/atmosphere interaction, to varying degrees of complexity, have been developed. These methods are grouped in regions II, III, and IV.

Region II has been labelled 'multiphase' models by most of the authors using this approach which was first presented by Larini et al. (1998) and subsequently used by Porterie et al. (2000), Zhou and Pereira (2000), Morvan and Dupuy (2001),Morvan et al. (2002b),Morvan et al. (2002a), Morvan and Dupuy (2004) and Dupuy and Morvan (2005) for flame spread through forest fuels. These models will be denoted MM, for multiphase models, in the following text. While the formulation of the MM is three-dimensional to date all MM studies have been implemented on two-dimensional grids. The largest reported computational domain size is 200 m wide and 50 m high; 200 s of simulated time required between 12 to 48 cpu hours on a single (2 GHz) processor (Dupuy and Morvan 2005). Since the MM results have been, to date, two-dimensional the complete fire/atmosphere interaction was not captured. For this reason they are placed along the vegetative fuel/fire boundary in Fig. 1. However, two-dimensionality allows relatively fine computational grids to be used and, therefore,

more complete models for the thermal degradation of the vegetative fuel, the subsequent combustion of pyrolysis vapors, and the local two-dimensional fire/atmosphere interaction. The computational cost due to the complexity of the physical models limits the application of the approach to medium-scale line fires (Morvan and Dupuy 2004).

Characteristic of the MMs in region II is that of Morvan and Dupuy (2004). They model fire spread through a vegetation complex consisting of thermally-thin shrubs, twigs, and grass. The solid fuel is approximated as a set of fixed fuel elements. The thermal (convective heat flux) and drag interaction of the solid fuel with the gaseous flow is accounted for by using coefficients from empirical correlations for representative shapes (cylinders, spheres, etc.). Moisture evaporation and pyrolysis are modeled with simplified temperature dependent mass loss rates. Arrhenius kinetics are used for char oxidation. Gas phase combustion kinetics are assumed to be infinitely fast, relative to the mixing of reactants, and the eddy dissipation model is used to determine gas-phase reaction rates. Thermal radiation in a multiphase medium (where the volume fraction of solid vs. gas is accounted for) is solved with a Discrete Ordinates solver that accounts for thermal radiation transfer within the vegetation fuel complex. An evolution equation for the soot volume fraction is solved, and a re-normalization group (RNG) k-ϵ turbulence model is used. Minimum grid resolutions in the fuel bed were $\Delta x = 0.1$ m, $\Delta z = 0.03$ m.

Region II also includes the simulations of Grishin and collaborators (e.g., Grishin et al. (1985); Grishin (1996)). The formulation of the model equations is very general, including solid pyrolysis, gas phase chemistry, and thermal radiation. However, it is unclear how these models are implemented and whether or not the reported simulation results, which span a 23 m long by 15 m high domain, are two or three dimensional (Grishin 1996). A $k - \epsilon$ turbulence model and P1 approximation for thermal radiation were used.

The methods in region III include those developed by Costa et al. (1995), Clark et al. (1996), Coen (2003), and Clark et al. (2003, 2004), all of which obtain the heat and moisture release, fuel consumption, and fire spread rate from either a prescribed formula or semi-empirical relations. For this reason, computational resources can be devoted to resolving atmospheric physics. For example, in the approach of Clark and colleagues (which is denoted by NCAR on Fig. 1 since its development began at the National Center for Atmospheric Research in the U.S.), a time dependent three–dimensional, non–hydrostatic, cloud–resolving numerical prediction model for the atmosphere is used. The cloud–resolving model can include vertically–stretched and terrain-following coordinates, and multilevel grid nesting. A recently reported application of this approach is Coen (2005). Fire spread rates are obtained from the semi-empirical Rothermel (1972) formulas. Sensible and latent heats from the fire are distributed vertically with an exponential decay over an assumed height. These approaches provide a first approximation to the fire/atmosphere coupling, especially suitable to large scale simulations on coarse grids (from a combustion physics point of view). On Fig. 1 BlueSky refers to the modeling framework developed by the US Forest Service for smoke transport from forest, agricultural, and range fires across regional scales (BlueSky 2004).

Region IV includes three-dimensional simulations that have physics-based models for the vegetative fuel, the atmosphere, and the fire. Linn and colleagues have developed a model called FIRETEC (Linn 1997; Linn et al. 2002; Linn and Cunningham 2005). FIRETEC was designed to operate over landscape scales (100s of meters) of flat or complex terrain. The three-dimensional nature of the model and its focus on the coupling between the atmosphere and fire constrain the ability of this model to use far sub-meter resolution over domains more than 300 m in all directions (Linn 2005). Thus, the fine-scale turbulence and combustion processes can not be resolved directly and must be approximated with subgrid models. In fact, any three dimensional simulation, run on present day computational platforms, of full scale fires requires subgrid models (including WFDS).

The governing model equations in FIRETEC are based on ensemble averaging, in a manner

similar to Reynolds averaging, of the conservation equations for mass, momentum, energy, and chemical species. This results in additional closure equations which require a number of turbulence modeling assumptions. FIRETEC is coupled to an atmospheric model HIGRAD (Reisner et al. 2000). The numerical time stepping scheme explicitly handles the high frequency acoustic waves. Thermal radiation transfer is computed using a diffusional transport approximation adapted from Stephens (1984). The chemical heat release from combustion occurs only in computational grid cells that contain the solid fuel (Linn et al. 2002). For grid cell dimensions that are smaller than the flame length this is unrealistic and improvements are underway (Colman and Linn 2003, 2005). A rate of heat release is determined from a universal reaction rate that is a function of the density of both the solid fuel and the gas phase, and an assumed Gaussian–shaped probability density function (PDF) of the temperature within a grid cell. The use of this PDF is physically motivated by the assumption that in general there are wide variations in temperature within a grid cell which are not sufficiently represented by the resolved temperature. The heat release rate, determined from the universal reaction rate and a heat of combustion of the volatiles, is partitioned between the gas and the solid (Linn et al. 2002). In both the gas and the solid phase energy equations these terms are exothermic. A weight factor is applied to these exothermic terms. In the solid phase energy equation the weight factor increases as the solid burns away; in the gas phase energy equation the weight factor has the opposite trend. For example, the weight factor that determines how much energy is returned to the solid fuel ranges from 25% to 75%; the highest value is applied when oxygen is abundant and more than 60% of the solid fuel mass is gone (Linn 2005). The motivation for this approach is to account for the progression from flaming to non-flaming combustion and to model the unresolved subgrid heat transfer processes in the vicinity of the fire.

Compared to the MM approach (which more directly solves the governing equations on more highly resolved two-dimensional computational grids) FIRETEC currently relies more on heuristic, physically-motivated assumptions, such as a prescribed subgrid probability distribution of the temperature in a grid cell and a rule for partitioning the energy release rate into the gas and solid phase equations. Many of these assumptions are driven by the limitations on spatial resolution in FIRETEC.

3 Overview of WFDS modeling approach

This section is an overview of the WFDS modeling approach. A detailed description of the model equations for the gas phase and vegetative fuel is given in Appendix A. The approach is similar to the MM approach described above (e.g., Porterie et al. (1998)) because separate but coupled models for the thermal degradation of the solid fuel and gas phase combustion are employed. This allows for a straightforward use of some of the physics-based solid phase models in region I of Fig. 1. As discussed above, these fuel driven models use an assumed flame geometry and temperature. Thus, in place of a constant heat flux on the solid fuel from an assumed flame, a transient heat flux (both convective and radiative) is used. This heat flux results from the local fire/atmosphere interaction as determined by the numerical solution of the conservation equations for momentum, total mass, energy, and the major species. Combustion is modeled with a mixture fraction based approach.

Unlike the MM approach, which is limited to two dimensional grids, WFDS can simulate fires in two or three dimensions (only fully three-dimensional simulations, with no symmetry assumptions, are reported here). Since three-dimensional simulations require significantly more computational resources, WFDS grids are coarser than those used in the MM approach. As a result, a combustion modeling approach appropriate for computational grids that significantly under-resolve the combustion zone must be used. The approach used here is described in Appendix A. Compared

to FIRETEC, which also operates on coarse grids (relative to the MM approach), WFDS more directly solves the equations governing the interaction of the fire/fuel and fire/atmosphere, relying less on heuristic physically motivated assumptions to include physical processes. For example, the thermal degradation of the solid fuel is driven solely by the resolved net heat flux on the fuel. In FIRETEC an additional amount of energy, a fraction of heat released by a combined solid-gas reaction, is deposited in the solid fuel (Linn and Cunningham 2005).

The basis of the surface vegetation model in WFDS is the physical assumption that combustion (i.e., heat release) occurs predominantly above the surface fuel bed. This is consistent with flame heights above the fuel bed that are significantly larger than the height of the fuel bed itself. With this assumption, two computational grids can be used: one for the gas phase that resolves the fire plume and another for the vegetative fuel bed that resolves heat transfer and thermal degradation. The fire plume can be resolved on a much coarser grid than the thermal degradation of the vegetation. The equations solved and numerical method employed in the gas phase calculation are essentially those used by FDS McGrattan (2005); details are in the appendix. The vegetation is "seen" by the gas phase as a source of momentum drag and heat and mass fluxes along the bottom boundary of the gas phase. Heat flux from the fire and the flux of fuel gas (from pyrolysis) both occur along the upper boundary of the grid for the vegetative fuel bed. A method that is similar to the multiphase approach discussed previously is then used to model the evolution of solid phase. Gas phase temperatures in the fuel bed are obtained from the gas phase computational grid directly above. The approach is described in more detail in the appendix. Note that this approach is less valid for vegetative fuels through which significant vertical flame spread and air flow can occur (such as through tree crowns). For the Australian grassland fire experiments simulated here the observed flame heights above the fuel bed were approximately 4 times the height of the fuel bed. An alternate modeling for raised fuels has been developed and is being validated. Preliminary results from this approach can be found at Mell et al. (2006).

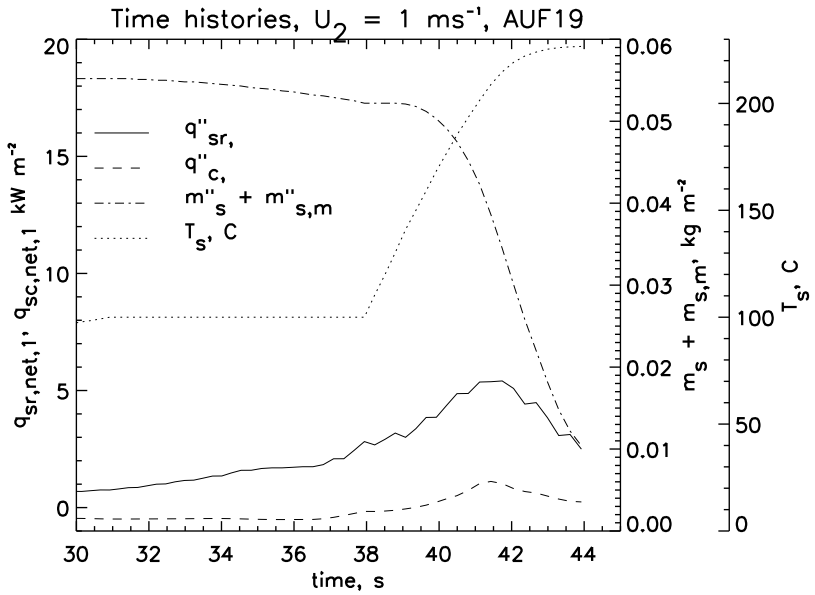

(a)

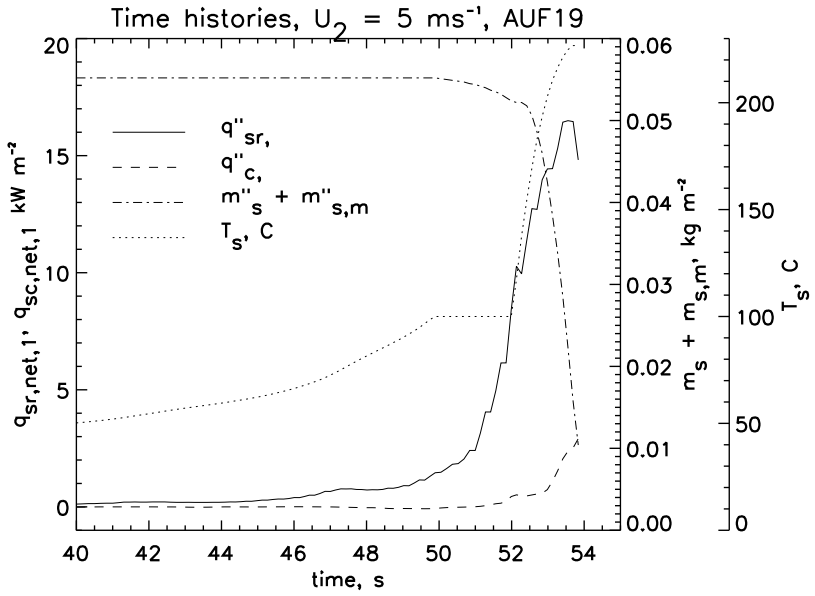

(b)

Figure 2: Time history of quantities in the uppermost layer of the grassland fuel model for two different ambient wind speeds at 2 m above ground; $U_2 = 1$ m s^{-1} in Fig. (a) and $U_2 = 5$ m s^{-1} in Fig. (b). In each figure the following are plotted: the convective ($\dot{q}''_{\rm c}$) and net radiative ($\dot{q}''_{\rm sr}$) fluxes on the top of the layer and the temperature ($T_{\rm s}$) and net mass loading (dry and moisture mass, $m''_{\rm s} + m''_{\rm s,m}$) of the layer.

Figure 2 shows the time history of a number of solid phase quantities, in the uppermost layer of the solid fuel model, for two different wind speeds: in Fig. 2(a) $U_2 = 1$ m s^{-1} and in Fig. 2(b) $U_2 = 5$ m s^{-1}, where U_2 is the wind speed 2 m above the ground. The grassland fuel properties measured in experiment F19 conducted in Australia were used (see Table 1; details of this experiment are given in Sec. 4.6). The time interval in each plot is 15 s. In the slower wind case, Fig. 2(a), 15 s is the time required for evaporation of the fuel moisture ($T_s = 100$ C) and the subsequent pyrolysis of the solid fuel (leaving only char). At this point in the model development char oxidation (smoldering combustion) is not accounted for. In Fig. 2(b) boiling and pyrolysis occur over a shorter time interval of 4 s, due to the higher heat fluxes on the solid fuel. The peak heat fluxes are over a factor of two larger in the higher wind case. The higher wind forces both the flame and the hot fire plume closer to the downwind fuel bed, increasing both the radiative and convective heat fluxes. This is a well known process leading to faster fire spread in stronger winds. For both wind speeds, radiation is the dominant heat transfer mechanism. In the simulations of Morvan and Dupuy (2004) the relevance of convective heat transfer was found to increase with increasing wind speed, eventually becoming the dominant mode of heat transfer. Their two-dimensional simulations use significantly smaller gas-phase grid cells ($\mathcal{O}(10)$ cm compared to $\mathcal{O}(1)$ m) resulting in much higher, and more realistic, gas phase temperatures in the fire plume. As a result, convective heat transfer into the solid fuel in regions of active combustion are underestimated in WFDS. This is an area of further model development. However, as will be seen below, WFDS does reproduce many experimentally observed fire spread trends.

4 Results

4.1 Overview of grassland fire experiments

Experiments were conducted on a 2500 ha (25,000,000 m^2) site in the Northern Territory of Australia, during July and August 1986 (Cheney et al. 1993; Cheney and Gould 1995). Fuels were open grasslands, and grasses were continuous, and normally fully cured. The site was divided into 170 plots, that were 100 m x 100 m, 200 m x 200 m, or 200 m x 300 m in size. A total of 121 of these grassland fires was used by Cheney et al. (1993) to examine the influence of fuel and wind on the spread rate of the head fire, R. Each fire travelled over flat terrain.

Plots contained one of two distinct grass types: *Eriachne burkittii* (kerosene grass), a coarser grass, with a mean surface–area–to–volume ratio of 9770 m^{-1}; and *Themeda australis* (kangaroo grass), a finer grass, with a mean surface–area–to–volume ratio of 12240 m^{-1}. Selected plots were harvested to alter the height h_s (m), load w_s (kg m^{-2}), and bulk density ρ_{sb} (kg m^{-3}) of the fuel. Plots were either natural or cut at 25 to 50 percent of natural grass height. The cut fuels either remained or were removed. A characteristic h_s, w_s, and ρ_{sb} were determined for each plot, and only plots with fairly even fuel load and continuous fuels were included in the analysis. Moisture content of the grass fuel, M, as a fraction of the oven dried weight of the grass was measured (here M is expressed as a percentage).

Wind speeds at 2 m and 10 m AGL (Above Ground Level) were measured in the open area immediately upwind and within 800 m of each fire. Wind speeds at 2 m AGL at each corner of the experimental plot were also measured at 5 s intervals for the duration of the fire. Wind orientation was not measured, only the speed of the horizontal wind. Ignition by field workers carrying drip torches started at the mid-point of a measured line and moved rapidly toward each end along the upwind edge of the grass plot. Thus, the fire could not spread upwind. Ignition lines were nominally 50 m long on 100 m x 100 m plots, and up to 175 m long on the larger plots. Ignition line fires were oriented at right angles to the prevailing wind direction. The average forward rate of spread

R (m s^{-1}) was determined over the longest period of spread before a substantial change in the rate of spread.

4.2 Overview of the numerical simulations

A number of simulations, with ignition line-fires of varying length ($L_{\rm ig}$), depth ($d_{\rm ig}$), and wind speed 2 m above the ground (U_2) were conducted to assess how well WFDS predicts the spread rate of the head fire. Two additional simulations, of specific Australian grassland experiments (F18 and C064, in Table 1), were run to evaluate WFDS predictions of the behavior of the entire fire perimeter.

The physical parameters required by the model are listed in Table 1 for both the gas phase and the vegetative fuel. Whenever possible, values obtained from the grass fire experiments are used. Properties that were not measured in the field were determined from literature sources for similar conditions (see Table 1). All boundaries except the inflow and bottom are open. At the open boundaries the density and mixture fraction have zero gradient conditions; velocity and pressure boundary conditions are described in McGrattan (2005).

Initially, throughout the domain and at the inflow boundary for the duration of the simulation, the dependence of the ambient wind with height above the ground, z, is defined to follow a power law:

$$U(z) = U_{2,\rm i}(z/2)^{1/7}. \tag{1}$$

Here $U_{2,\rm i}$ is the value in WFDS of the initial wind speed at a height of 2 m. This expression is suitable for smooth terrain and has been used in simulations of fire spread in pine needle beds (Morvan and Dupuy 2001) and in a grass/shrub fuel bed (Morvan and Dupuy 2004). Other ambient wind profiles can easily be implemented but their influence on simulated fire behavior will be investigated elsewhere (e.g., Mell et al. (2005)). In general, U_2 can be modified by drag from surface vegetation and the fire plume (due to both entrainment and blockage effects). When comparing head fire spread rates from WFDS and the experiments over a range of conditions a consistent measure of the representative ambient wind speed U_2 must be used. The experimental value of U_2 was determined by averaging, over the time interval spanning ignition to when the fire reached the downwind firebreak, the measured horizontal wind speed at the two upwind corners of the plot (see Fig. 3). The simulated value of U_2 was determined by averaging, over the same time interval used to compute the experimental U_2, the horizontal wind speed in the grid cell located at the center of the ignition line fire and at a height of $z \cong 2$ m. For the simulations reported here this velocity location was within a height range of $z = 1.95$ m to 2.1 m. The magnitude of the crosswind velocity, v, in WFDS was initially zero and remained much smaller than u so that $\sqrt{u^2 + v^2} \cong u$. The corner values of the simulated velocity were not used to define U_2 in the simulations because they were not representative (they were too low due to drag from unburned vegetation) of the wind speed upwind of the head fire.

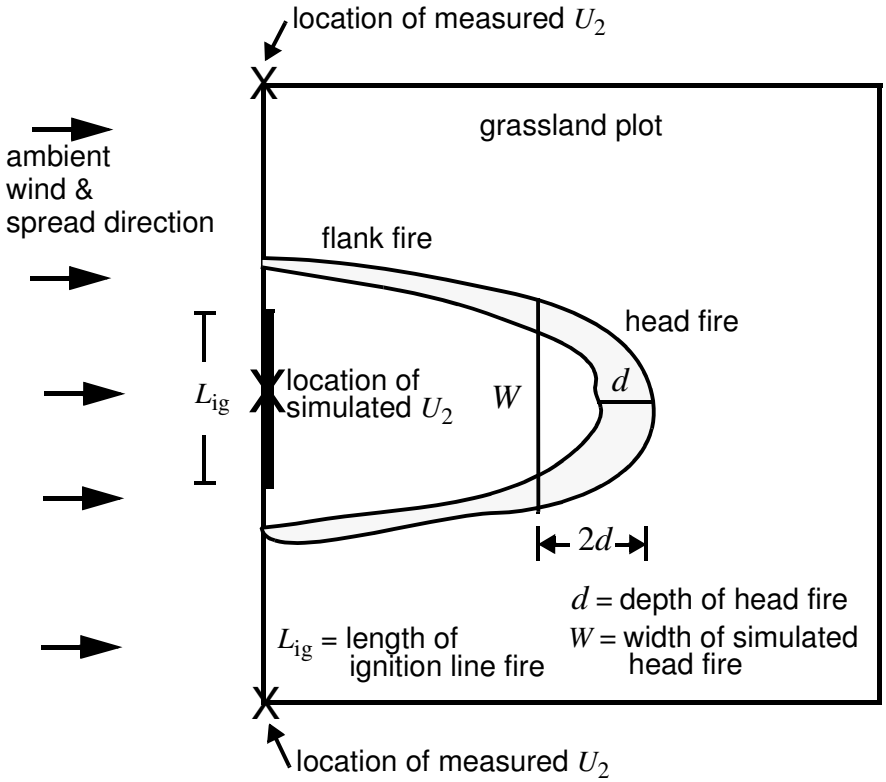

Figure 3: A schematic of a grassland fire. The ambient wind flows from left to right. The value of the wind speed, U_2, in the experiments is obtained by averaging the magnitude of the horizontal velocity measured at a height of $z = 2$ m positioned at the upper and lower left-hand-side corners of the grassland plot. The value of the wind speed in the simulation is obtained from the computed component of the velocity vector parallel to the ambient wind at a height of $z \approx 2$ m positioned above the center of the ignition line fire.

The heat release rate per unit area of an ignition line fire has two components: the burning grass and the hydrocarbon fuel deposited by the drip torches. The hydrocarbon fuel was assumed to be gasoline (heat of combustion 32 MJ L^{-1}) deposited with an area density of 0.25 L m^{-2}. Complete burning of the gasoline and grass fuel was assumed to occur over a time interval equal to d_{ig}/R_{ig} where $R_{ig} = 0.3$ m s^{-1} is assumed (based on experimental head fire spread rates). For example, in simulations using the grassland fuel present in experiment F19 (see Table 1) an ignition line fire of depth $d_{ig} = 3.3$ m had a duration of 11 s and a heat release rate per area of 1460 kJ m^{-2}. The ignition procedure, which can be easily modified, will affect the initial behavior of the fire. Since the information available for the field ignition method was incomplete (e.g., it is unknown how much liquid fuel was distributed on the grass) the method used here is a best estimate to the field procedure.

Care must be taken to avoid nonphysical numerical boundary affects. A fire entrains the sur-

rounding ambient air into its rising plume. The numerical boundaries must not interfere with this process in a significant way. For example, when the inflow boundary (at which the wind speed is held fixed) is too close to the fire, entrainment from the upwind direction is reduced. This can have significant effects for sufficiently low ambient wind speeds. In reality, under such conditions entrainment by a fire plume in an unbounded domain can add to the ambient wind oriented into the head fire. In numerical simulations with upwind boundaries that are too close to the fire, the flame spread rate increases as the boundary is moved further from the fire.

It was found that spread rates and fire behavior were nearly identical when the grassland plot was centered in a 1500 m versus a 2700 m square domain. In the simulations discussed below, therefore, the fires occurred within a 300 m by 300 m plot surrounded by a 600 m border on all sides (1500 m by 1500 m area). A number of tests were made to check the influence of grid resolution on head fire spread rates. In these tests the sizes of horizontal grid cells were $\Delta x = \Delta y = 1$ m, 1.66 m, or 3.33 m. As the grid resolution increased, the head fire spread rate decreased somewhat. Spread rates with the $\Delta x = 1$ m were 15% (or less) slower than the $\Delta x = 3.33$ m cases and 10% (or less) slower than $\Delta x = 1.66$ m cases. Table 2 contains the values for grid resolution and other parameters for the productions simulation runs.

Production simulations (1500 m $\times$ 1500 m $\times$ 200 m, in general) required 16 million grid cells and 11 processors. The total cpu time required for these runs depended on the overall heat release, which increases with fuel loading. For most of the cases considered 44 cpu hours were needed for 100 s simulated time (i.e., all 11 processors running for 44 hours on 1.8 GHz processors). Exploratory simulations run much faster, on the order of 2 hours on a single processor. These faster runs were on smaller domains and provide reasonable results if the ambient wind speed is sufficiently high. For lower ambient wind speeds ($\mathcal{O}(1)$ m s^{-1}) natural entrainment was influenced by the presence of numerical boundaries as discussed above. Thus, for consistency all simulations had horizontal domains of 1500 m $\times$ 1500 m.

It should be noted that the results of any large scale simulation will depend on both the grid resolution and the modeling assumptions employed. Fully resolving the combustion zone (as captured by the relatively simple fast-chemistry mixture fraction approximation used here) requires sub-millimeter grid resolution (Mell et al. 1996). The larger scale fire/fuel interactions, which control the heat transfer to the fire bed, occur on scales on the order of 1 m to 10 m for grass fires, a factor of over a thousand greater. Fire/atmosphere interactions occur over even larger scales. Present day computers (even massively parallel platforms containing thousands of processors) do not have the memory capacity or processor speeds to fully resolve processes occurring from the combustion zone up to scales that characterize the fire/atmosphere interactions. For this reason, the governing equations must be approximated in a way that retains the physical processes that are most relevant to the fire problems under study. Here the emphasis is placed on resolving the larger scale fire plume dynamics and heat transfer processes, in the fire/fuel and fire/atmosphere interactions, that drive fire spread (as opposed to smaller scale combustion processes of, for example, chemical kinetics and soot generation). In the following sections WFDS will be evaluated by determining how well it reproduces observed fire-spread trends in the Australian grassland experiments.

A characteristic example of both the experiment and simulation is shown in Fig. 4. A photograph of the fire perimeter taken during experiment F19 is shown in Fig. 4(a). A rendering of the simulated fire front and smoke plume using the visualization tool Smokeview (Forney and McGrattan 2004) is plotted in Fig. 4(b). As discussed above, smoldering combustion is not currently modeled. For this reason, there is no smoke generated upwind of the fire in the simulation (Fig. 4(b)).

(a)

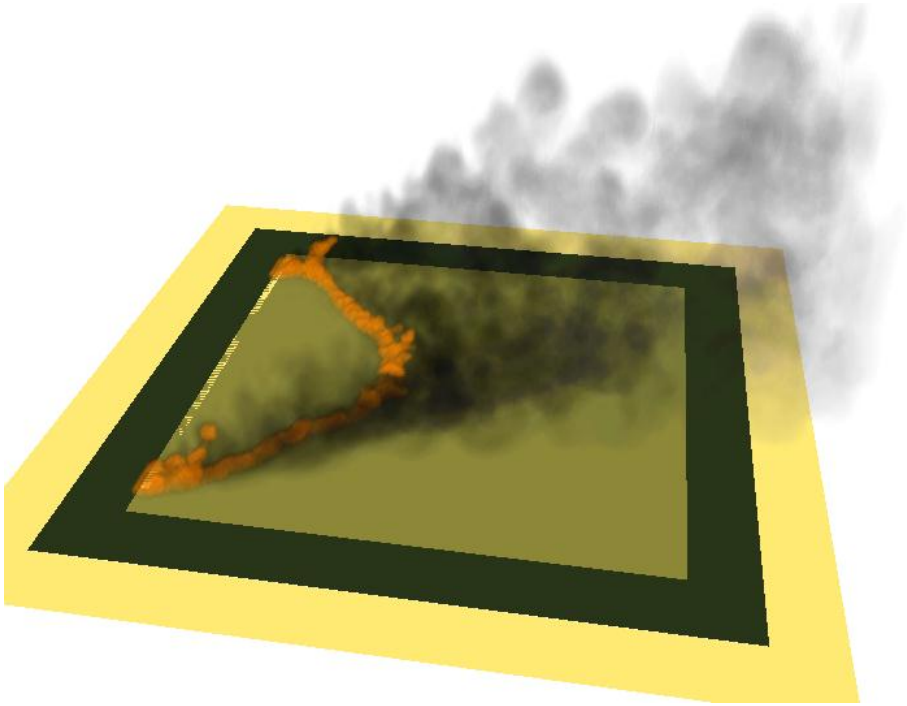

(b)

Figure 4: **(a)** Photograph of experimental fire F19 at $t = 56$ s. **(b)** Snapshot of WFDS simulation of experimental fire F19 at $t = 56$ s.

4.3 Effect of wind on head fire spread

Cheney et al. (1993) found that when head fire spread rate was correlated with fuel type, wind speed, and fireshape variables, wind speed U_2 had the most effect on the spread rate. Convective activity was thought to be a primary factor that determined whether fires progressed steadily in the direction of the prevailing wind, and fires burning under light wind conditions often spread erratically as they responded to gust and lulls caused by the localized thermal activity. As the wind speed increased, the head fire width required for fires to approach their potential quasi–steady rate–of–forward spread, R_s, also increased. Cheney et al. (1993) note that the wind directly influencing fire spread is the net wind at the flame zone, not the wind measured remote from the fire. However, since this net wind speed is not known and would be very difficult to measure, empirical formulas for the spread rate of the head fire are based on a representative ambient wind U_2. The determination of U_2 was discussed in Sec. 4.2.

The following empirically based formula (Eq. 4 in Cheney et al. (1998)) relates the experimentally observed head fire spread rate R_o (m s^{-1}), to the measured wind speed U_2, the head fire width W (m), and the fuel moisture content M (%):

$$R_\mathrm{o} = (0.165 + 0.534U_2)\exp(\{-0.859 - 2.036U_2\}/W)\exp(-0.108M). \tag{2}$$

They defined the head fire width, W, as the width of the fire, measured at right angles to the direction of head spread, which influenced the shape and size of the head fire during the next period of spread measurement (Cheney and Gould 1995). The effective width of the head fire can also be defined as that portion of the perimeter where the flames are leaning towards unburnt fuel. In WFDS the head fire width was defined to be the distance between the flank fires one fire depth upwind of the trailing edge of the head fire (see Fig. 3). With increasing head fire width, $W \to \infty$, the head fire spread rate, Eq. (2), increases and asymptotes to a potential quasi-steady spread rate (Cheney et al. 1998):

$$R_\mathrm{s} = (0.165 + 0.534U_2)\exp(-0.108M) \tag{3}$$

In the figures to follow, simulated head fire spread rates and head fire location were compared to their experimentally observed values through the use of these empirical spread rate relations.

Simulations using four different ignition line fires, L_ig = 8 m, 25 m, 50 m, 100 m, and four wind speeds, U_2 = 1 m s^{-1}, 3 m s^{-1}, 4 m s^{-1}, 5 m s^{-1} (16 simulations in all) were run. See Table 2 for a summary of the simulations. For each case the line fire was ignited simultaneously along its entire length. The fuel bed parameters of experiment F19 (see Table 1) were used. The wind speeds used are such that the fire-atmosphere interaction ranges from a more plume dominated fire to a wind dominated fire (Pagni and Peterson 1973; Pitts 1991). Figure 5(a) shows the more plume dominated case (U_2 = 1 m s^{-1}). In this figure the plume rise close to the ground ($z < 20$ m) is dominated by buoyancy resulting in a nearly vertical rise. In Fig. 5(b) the wind (U_2 = 5 m s^{-1}) dominates the plume rise. As shown previously in Fig. 2 the net heat flux to the solid fuel is significantly higher for the faster wind speed case due to flame tilt toward the unburned fuel bed.

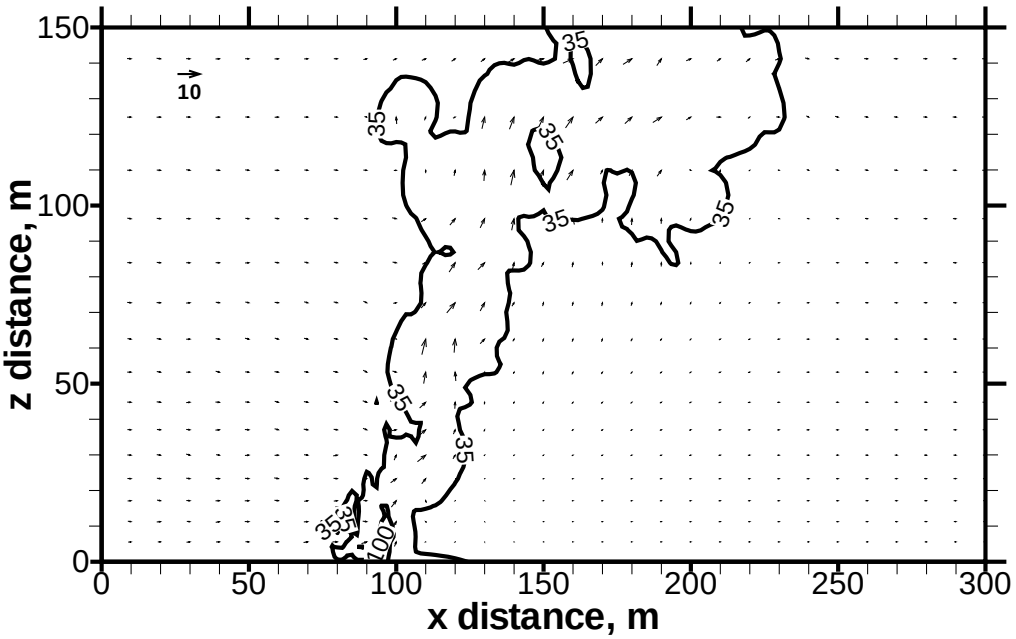

(a)

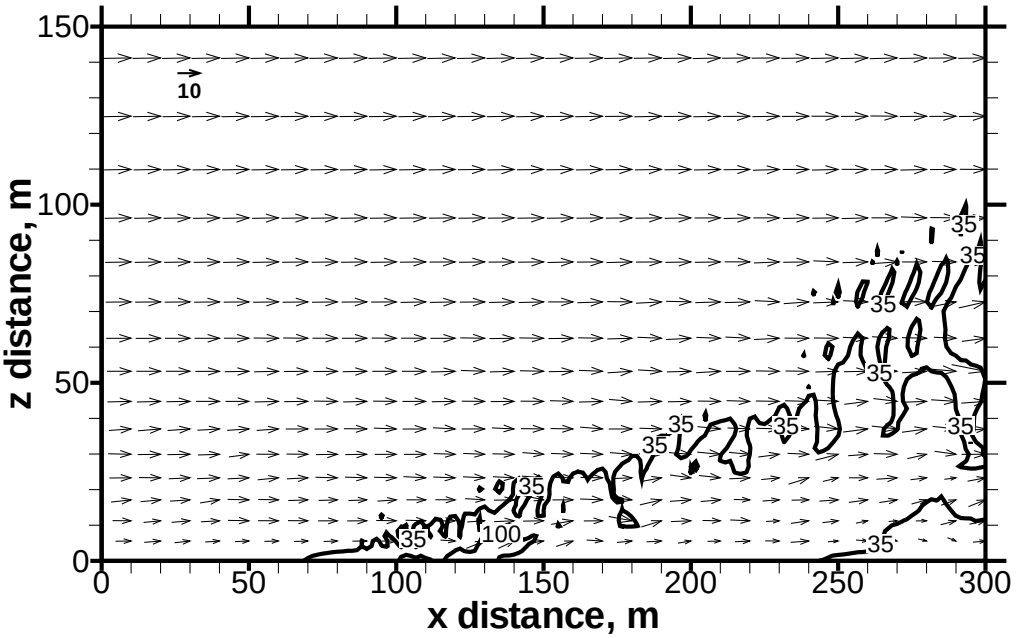

(b)

Figure 5: Temperature contours (35 °C and °100 C) and velocity vectors in a x-z plane for fires spreading in a grassland fuel bed with the characteristics of experiment F19 (see Table 1). The length of the ignition line fire was $L_{\rm ig} = 50$ m. The two figures correspond to two different wind speeds: **(a)** $U_2 = 1$ m s^{-1} at $t = 100$ s; **(b)** $U_2 = 5$ m s^{-1} at $t = 50$ s. Horizontal spacing of vectors is 10 m (every sixth grid cell); vertical spacing varies because grid is stretched (every fourth cell is shown). The depth of the ignition line fire is approximately 7 m and is located at $x = 50$ m to 57 m.

Figure 6 is a plot of head fire spread rate versus wind speed. Spread rates from WFDS (symbols), BehavePlus (Andrews et al. 2003) (solid line) and the empirically derived quasi-steady spread rate form of Eq. (3) (i.e., $W \to \infty$) (dashed line) are shown. The spread rate from WFDS was obtained from the time history of the leading edge of the head fire. The leading edge was identified by the location of non-zero fuel mass loss rate, along the centerline of the grass plot, that was furthest downwind. As is seen in Fig. 7, WFDS spread rates for $L_{\rm ig} = 50$ m quickly reach a quasi-steady value. The dependence of the spread rate on the wind speed is well predicted by WFDS. The quantitative agreement of WFDS is also good, however it is important to note that the sensitivity of WFDS to realistic variations in environmental variables (wind speed, moisture content, etc.) has not yet been assessed. Another important issue is how the value of the wind speed, U_2, is obtained.

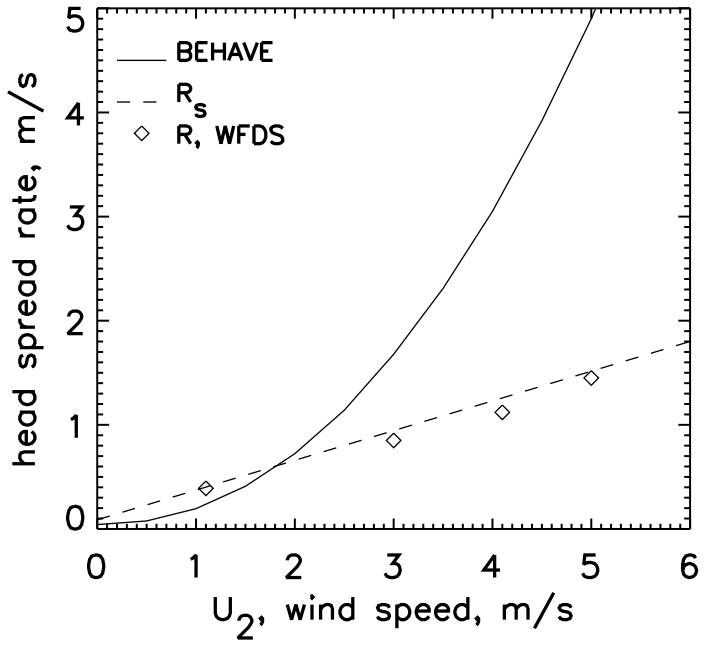

Figure 6: Spread rate of head fire versus the wind speed at a height of 2 m. Symbols are WFDS; solid line denoted BEHAVE is from the BehavePlus computer; program developed by the USDA Forest Service, and dashed line is the empirical expression, Eq. 3, from the grassland fire experiments (i.e., Eq. (4) in Cheney et al. (1998) with $W \to \infty$) .

As discussed in the previous section, both Eq. 2 and Eq. 3 and the WFDS inflow boundary condition use a value of U_2 that is the average wind speed at a height of approximately 2 m. In BehavePlus the default height of the wind speed is at the mid-flame height. The experimentally observed average mid-flame height, for $U_2 = 4.8$ m s^{-1}, was 1.3 m for this fuel and the mid-flame wind speed was 4.5 m s^{-1}. With $U_2 = 4.8$ m s^{-1} input into BehavePlus for the mid-flame wind speed R is 4.4 m s^{-1} (this plotted in Fig. 7). With the observed value of 4.5 m s^{-1} for the mid-flame wind speed input into BehavePlus R is 3.9 m s^{-1}. This still significantly over predicts the empirically determined spread rate of the head fire, which is $R = 1.4$ m s^{-1}The over prediction of the spread rate by Behave for fuels with a surface-to-volume ratio of 13100 m^{-1}, which is similar to the fuel used here ($\sigma = 12240$ m^{-1}) has been noted before (Gould (1988)).

4.4 Effect of fire head width on fire spread

After U_2, the head-fire width, W, was observed to account for the greatest variation in spread rate in the grassland experiments. The correlation between R and the measured moisture content of dead grass M was not significant. This was attributed to difficulties with sampling and handling techniques of M, the relatively small range of M during the experiments, and to the large effect of wind speed masking the effect of moisture content. Cheney and Gould (1995) found that R_o, for a given U_2, rapidly increased as W increased. For lower wind speeds ($U_2 < 3.5$ ms^{-1}), R_o appeared to asymptote when $W \cong 50$ m. For $U_2 > 3.5$ ms^{-1} both R_s and the value of W at which $R_o \approx R_s$ increased. Cheney et al. (1993) comment that models developed from experimental fires that have not been allowed to burn to a substantial size ($W > 100$ m) are likely to under predict the spread rates of wildfires, particularly at higher wind speeds. Figure 7 shows the head fire spread rate

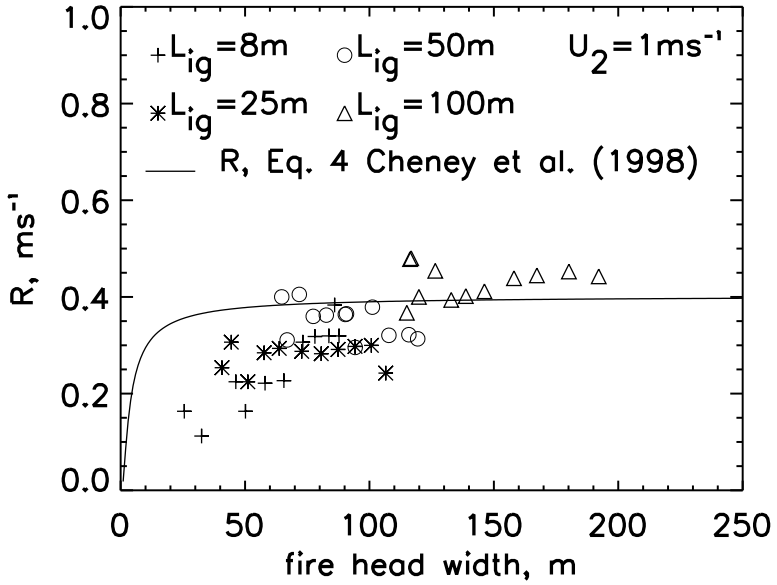

Figure 7: Spread rate of head fire versus the width of the head fire. The wind speed is $U_2 = 1$ m s^{-1}. Spread rates from four different lengths of the ignition line fire ($L_{ig} = 8$ m, 25 m, 50 m, 100 m) are shown. Symbols are WFDS; solid line is determined using the empirical expression, Eq. (2), from the grassland fire experiments (Eq. (4) in Cheney et al. (1998)).

versus the head fire width for $U_2 = 1$ m s^{-1} and the four different lengths of the ignition line fire, $L_{ig} = 8$ m, 25 m, 50 m and 100 m. The solid line is the spread rate from Eq. (2). The simulations reproduced the trend of an increasing head fire spread rate with an increasing width of the head fire. The head width increased monotonically with time (not shown). All ignition line length cases, with the possible exception of $L_{ig} = 8$ m, reach a quasi-steady spread rate that is within 25% of the Eq. (3) value. Longer ignition line cases reach spread rates that are closer to the Eq. (3) value (i.e., the plateau value of the solid line). The experimental fires, as described by Eq. (2), obtained a quasi-steady spread rate at narrower head fires than the simulated fires. Figure 8(a-d) are sequential snapshots of the burning region (shaded contours of the mass loss rate are shown) for each of the ignition line fire lengths used. Note that for the $L_{ig} = 50$ m and 100 m cases, Fig. 8(c,d) respectively, the flank fires reach the upper and lower fire breaks.

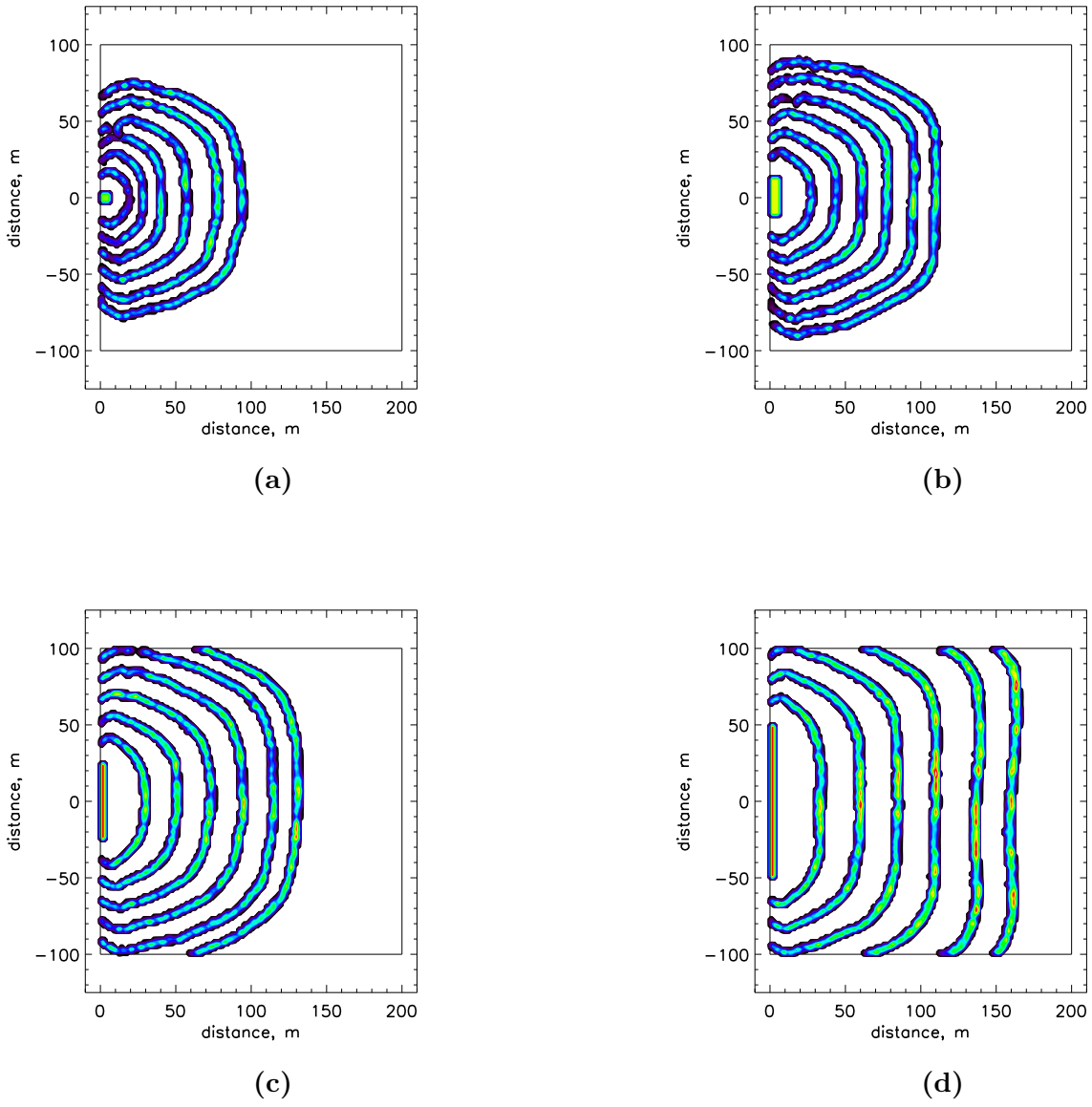

Figure 8: Time evolution of fire perimeters, shown as shaded contours of the mass loss rate, for $U_2 =$ 1 m s^{-1} and four different ignition line lengths $L_{\rm ig} = 8$ m, 25 m, 50 m, 100 m in Fig. (a), (b), (c) and (d) respectively. The fire perimeters are plotted at times $t = 0$ s, 60 s, 120 s, 180 s, 240 s, 300 s and 350 s. The fire spreads in a 200 m $\times$ 200 m grassland plot with the fuel properties of experiment F19 listed in Table 1

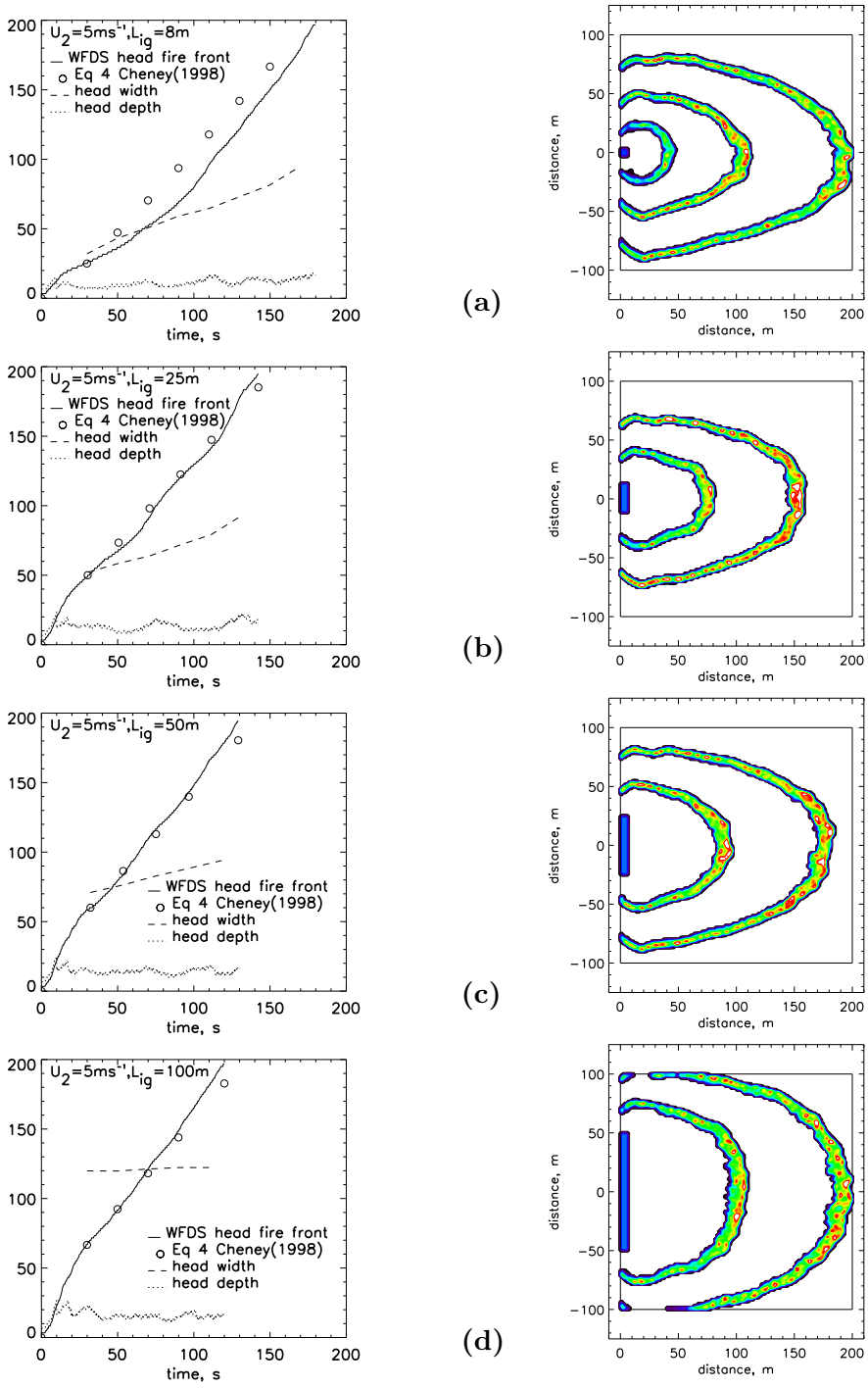

Figure 9: Left column shows the location of the leading edge of the head fire versus time from WFDS (solid line) and from using Eq. 2 (circles), an empirical formula for the quasi-steady spread. The wind speed is $U_2 = 5$ m s^{-1} and the four ignition line fires are used, $L_{\rm ig} = 8$ m (a), 25 m (b), 50 m (c), and 100 m (d) long (same $L_{\rm ig}$ as in Fig. 8). The width (dashed line) and depth (dotted line) of the head fire are also plotted. The fire perimeter (shaded contours of mass loss rate) for each case are shown in the right column at 60 s intervals, starting at 0 s The fire spreads in a 200 m $\times$ 200 m grassland plot with the fuel properties of experiment F19 listed in Table 1.

In Fig. 9, results with $U_2 = 5$ m s^{-1} are shown. In the left column the location of the leading edge of the head fire (solid line) versus time from WFDS is plotted. Each row in Fig. 9 corresponds to a different ignition line fire length. Also shown in the left column are the width (W, dashed line) and depth (d, dotted line) of the head fire. In each case an initial time period of relatively rapid spread is present, followed by a slower spread rate. This initial rapid spread may depend on the ignition procedure, and needs to be investigated. In order to compare to experimental fire behavior, the location of the head fire is also determined using the empirical relation, Eq. (2) (circles). This equation is implemented using W calculated by WFDS and $U_2 = 5$ m^{-1}. For the cases with $L_{\rm ig} =$ 25 m, 50 m, and 100 m WFDS predictions of the head fire location agree well, overall, with those derived from Eq. (2). At the latest time WFDS does over predict the location of the head fire, but by less than 8%. When $L_{\rm ig} = 8$ m there is an initial period of time, greater than 30 s, during which the head fire spread rate increases before reaching an more quasi-steady value after $t \cong 110$ s. The head width (dashed line) at which the simulated head fire spreads in a quasi-steady manner is approximately $W = 65$ m (note Fig. 7 shows similar results for $U_2 = 1$ m s^{-1}). This is consistent with experimental observations that spread rates are relatively unaffected by $L_{\rm ig}$ when $L_{\rm ig} > 75$ m and U_2 is sufficiently small. Relatively little change in the head fire width occurs for $L_{\rm ig} = 100$ m. Cheney and Gould (1995) note at their highest wind interval between 4.7 and 7.1 m s^{-1} a head fire width of more than 125 m in open grassland is required to get spread rates within 10 percent of the quasi-steady rate of spread. Thus, with an ignition line of 100 m, spread rates could still be increasing at wind speeds of 5 m s^{-1}. The oscillations in the location of the head fire and fire depth (most clearly seen Fig. 9(b) are due to interactions of the fire plume and the local wind field. Note that increases in R are associated with increases in d.

Figure 9 (right column) shows the fire perimeter at 60 s intervals. The relatively high wind speed results in head fire depths (10 m - 12 m) that are greater than the flank fire depths (5 m - 7 m). This does not occur in the weak wind case ($U_2 = 1$ m s^{-1} in Fig. 8). This behavior is consistent with field observations. The average head fire depth from field measurements for $L_{\rm ig} = 175$ m and $U_2 = 4.8$ m s^{-1} is $d = 10$ m. Observed fire depths were interpreted from oblique photographs which were rectified and plotted onto a planar map of time isopleths of fire perimeter and fire depth.

4.5 Residence time, mass flux, heat release rate

Figure 10 is a plot of the head fire residence time, τ, versus the spread rate of the head fire. Residence times from the WFDS simulations, Australian (AU) experiments, and an empirical formula from Anderson (1969) are plotted on the figure. In the empirical formula the residence time, $\tau \equiv dR^{-1}$, is a function only of the surface-to-volume ratio:

$$\tau \equiv \frac{d}{R} = \frac{75600}{\sigma_{\rm s}}. \tag{4}$$

Sneeuwjagt and Frandsen (1977) tested Eq. (4) and state it provided a good fit to data from their grassland fire experiments. The value of τ from Eq. (4), using $\sigma_{\rm s}$ for the two AU grassland experiments C064 and F19, is shown in Fig. 10 as horizontal lines labelled C064e and F19e. The value of $\sigma_{\rm s}$ is 9770 m^{-1} and 12240 m^{-1} for C064e and F19e, respectively (see Table 1). The value of τ based on measured values of d and R in the AU experiments are denoted by C064AU and F19AU. Symbols mark the value of τ from WFDS predictions of d and R for a range of $L_{\rm ig}$ and U_2 conditions with F19 grassland fuel. The value of the depth of the head fire, d, is in the direction of spread (see Fig. 3). C064s or CF19s denote WFDS results for conditions identical to the two AU experiments. WFDS values of τ are larger than those from Eq. (4); but only weakly dependent on R (especially for the larger $L_{\rm ig}$ values), which is consistent with Eq. (4).

An important implication of Eq. (4) is that the mass loss rate ($\dot{m}''_{\rm s}$, kg s^{-1}m^{-2}), and therefore the reaction intensity ($I_{\rm R}$, kW m^{-2}), averaged over the time interval τ are constant for a given $\sigma_{\rm s}$:

$$I_{\rm R} = \Delta h_{\rm c} \frac{1}{\tau} \int_0^{\tau} \dot{m}''_{\rm s} {\rm d}t = \frac{\Delta h_{\rm c}(1-\chi_{\rm char}) w_{\rm s}}{\tau} = \frac{\Delta h_{\rm c}(1-\chi_{\rm char}) w_{\rm s} \sigma_{\rm s}}{75600}. \quad (5)$$

The reaction intensity and the commonly used fireline intensity, I (kW m^{-1}), are also related:

$$I = I_{\rm R} d = I_{\rm R} R \tau = \Delta h_{\rm c}(1-\chi_{\rm char}) w_{\rm s} R, \quad (6)$$

where $\Delta h_{\rm c}(1-\chi_{\rm char}) w_{\rm s}$ is the heat per unit area released in the combustion process (neglecting heat from char oxidation). The fireline intensity has a number of practical uses since it has been related to observed flame heights and to fire management guidelines (e.g., Chandler et al. (1983)). By integrating I along the fire perimeter the total heat release rate, HRR (kW), for that portion of the perimeter can be found. Boundary conditions on large scale atmospheric models require values of HRR. Figure 11 shows the time history of WFDS predictions of $\dot{m}''_{\rm s}$ spatially averaged over the

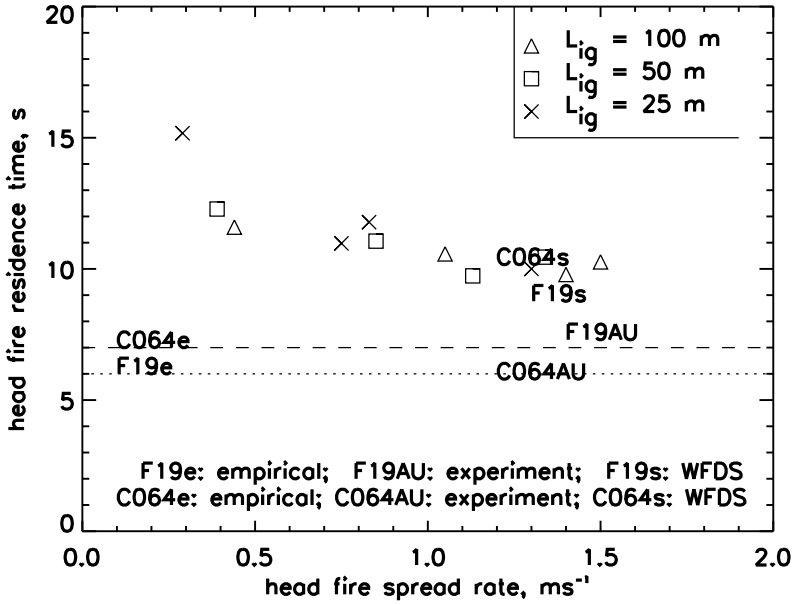

Figure 10: Residence time, τ (s), from a number of sources. Symbols are $\tau = dR^{-1}$ where d and R are determined from WFDS simulations with $L_{\rm ig}$ = 25 m, 50 m, 100 m during quasi-steady flame spread in a fuel bed with the characteristics of the F19 experiments. The dotted line (labelled 'F19e') and dashed line (labelled 'C064e') are residence times from the empirical formula Eq. (4) using $\sigma_{\rm s}$ from experiment F19 and C064 (see Table 1), respectively. F19s and C064s are $\tau = dR^{-1}$ values from WFDS simulations of experiments F19 and C064, respectively. F19AU and C064 are $\tau = dR^{-1}$ values from the experimentally measured d and R.

fire beds of the head fire, the flanking fires, and entire fire perimeter. Two different wind cases, each with $L_{\rm ig}$ = 100 m, are plotted: in Fig. 11(a) U_2 = 1 m s^{-1} and in Fig. 11(b) U_2 = 5 m s^{-1}. In each case, the average mass flux is largest in the head region of the fire perimeter, due to flame tilt. However, the flanking fires can be a greater portion of the entire fire line. This is the case for

$U_2 = 5$ m s^{-1} as seen in Fig. 9(d). The total mass flux varies within 15% of its mean value for most of the $U_2 = 1$ m s^{-1} case (after the fluctuations from ignition have died off) and for the latter half of the $U_2 = 5$ m s^{-1} case.

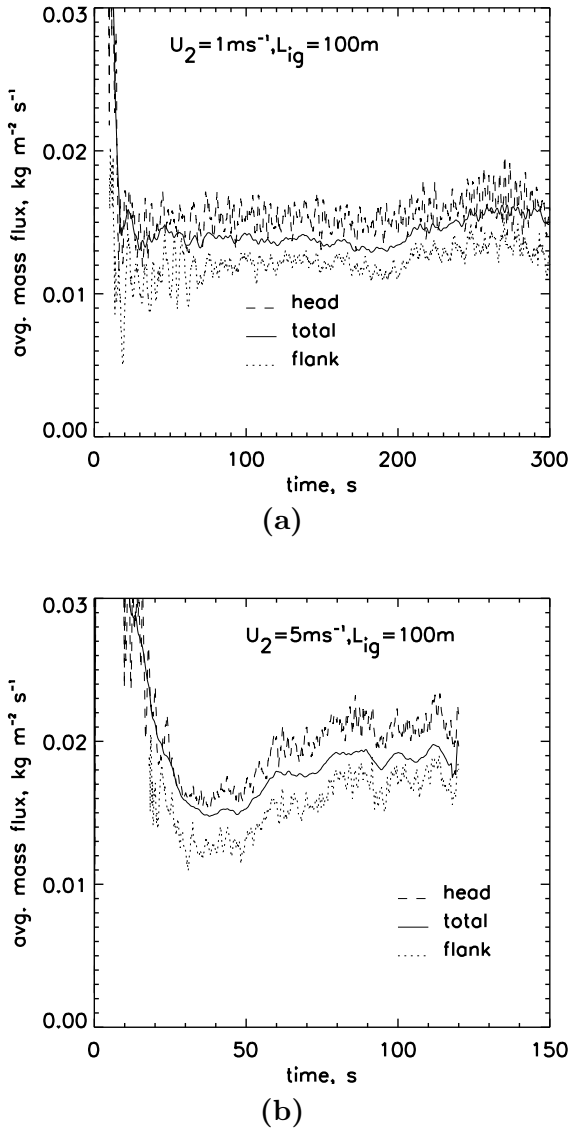

Figure 11: WFDS time histories of the mass flux of fuel gases during pyrolysis, $\dot{m}''_{\rm s,pyr}$ (kg m^{-2}s^{-1}), averaged over the head fire, flank fires, and the total fire perimeter. In both figures $L_{\rm ig} = 100$ m. In both figures the fuel bed has the characteristics of the grass in AU experiment F19 (Table 1). In **(a)** $U_2 = 1$ m s^{-1} and in **(b)** $U_2 = 5$ m s^{-1}.

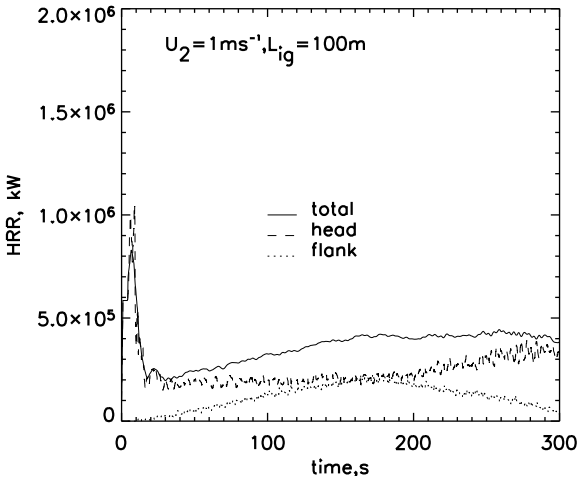

(a)

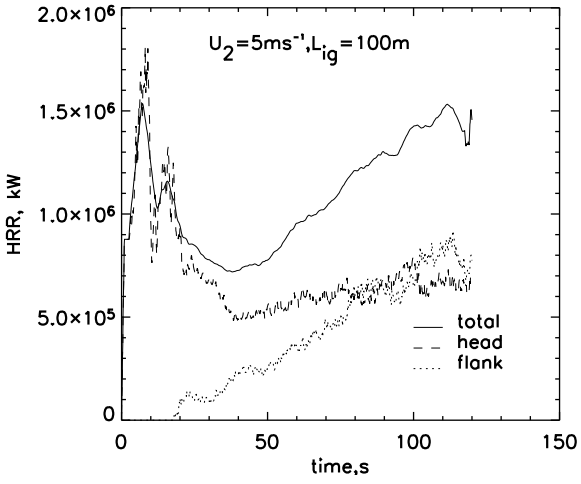

(b)

Figure 12: WFDS time histories of the heat release rate, HRR (kW), in the head fire, flank fires, and the total fire for the same cases shown in Fig. 11. In both figures $L_{\rm ig} = 100$ m. The fuel bed has the same characteristics as the grass in experiments F19 (Table 1). In **(a)** $U_2 = 1$ m s^{-1} and in **(b)** $U_2 = 5$ m s^{-1}.

The total HRR of the head fire, the flanking fires, and the entire fire bed for the same two cases is displayed in Fig. 12. These HRR values are computed by summing the mass fluxes over each region of the actively burning fireline:

$$HRR_{FR} = \int_{FR} I d\ell \cong \sum_{FR} \Delta h_c (1 - \chi_{\rm char}) \dot{m}''_s \Delta x \Delta y, \tag{7}$$

where FR denotes the head fire or flank fire region of the fire line and Δx, Δy are the horizontal dimensions of the grid. After the fire line reaches the edges of the grassland plot at approximately t = 180 s in the $U_2 = 1$ m s^{-1} case (see Fig. 8(d)) the flanking fires begin shortening and eventually disappear, no longer contributing to the HRR in Fig. 12(a). As the flanking fires shorten, the head fire lengthens and its HRR increases until, at $t = 350$ s, it spans nearly the entire 200 m grass plot. In Fig. 12(b) the stronger ambient wind lengthens the flanking fires (see Fig. 9(d)) causing their HRR (and therefore the total HRR) to increase over the latter part of the simulation.

4.6 Case studies

The mechanism of fire spread can change along the fire perimeter depending on the wind speed. In zero ambient wind, entrainment by the fire creates a local wind into which the entire fire line spreads (backing fire). In the presence of an ambient wind, the downwind portion of the fire perimeter spreads with the wind (heading fire), the upwind portion of the fire perimeter spreads into the wind (backing fire), and the sides or flanks of the fire perimeter spread under conditions that can alternate between heading and backing fires. Note that in the cases considered here, there are no backing fires since ignition occurred along the fire break at the upwind border of the plot. Backing fires, in which the flame tends to tilt away from the unburned fuel, can consume the fuel from the base upward, resulting in more complete fuel consumption. Heading fires, in which the flame tilts toward the unburned fuel, can be associated with lower fuel consumption because the grass ignites at the top and burns downward, covering the unburned fuel beneath with a protective coating of ash. The spread mechanism in a flank fire can involve, depending on the fire/wind interaction, both the burning downward mechanism of head fires and the burning upward mechanism of backing fires. Thus, modeling the evolution of the entire fire line is a greater challenge, due to the different spread mechanisms, than modeling the behavior of just the head fire.

WFDS can not directly resolve the details in the grass fuel bed that differentiate a backing fire from a heading fire since the entire fuel bed is unresolved on the gas phase computational grid. For example, the height of the first grid cell in WFDS simulations of experiment F19 is 1.4 m while the height of the grass is 0.51 m. However, the fire/atmosphere interactions that occur over larger scales are much better resolved. It is hoped that this level of resolution of the fire physics will be sufficient to capture the dynamics of the entire fire perimeter. It is important that a three-dimensional model predict the behavior of the entire fire perimeter. Otherwise, the overall heat release rate, fuel consumption, and smoke generation will be (to some degree) incorrectly predicted. The potential for this was seen, for example, in Fig. 12(b) where the gradual lengthening of the flank fire increased the total HRR of the fire while the HRR contribution from the head fire remained constant. These global fire characteristics are particularly important inputs to landscape and regional smoke transport models, which do not attempt to model the fire/fuel physics. In addition, the mechanisms behind extreme fire behavior (such as blow ups) are still poorly understood. A model that simulates the behavior of the entire fire perimeter, as opposed to only the head fire, is more likely to shed light on these issues.

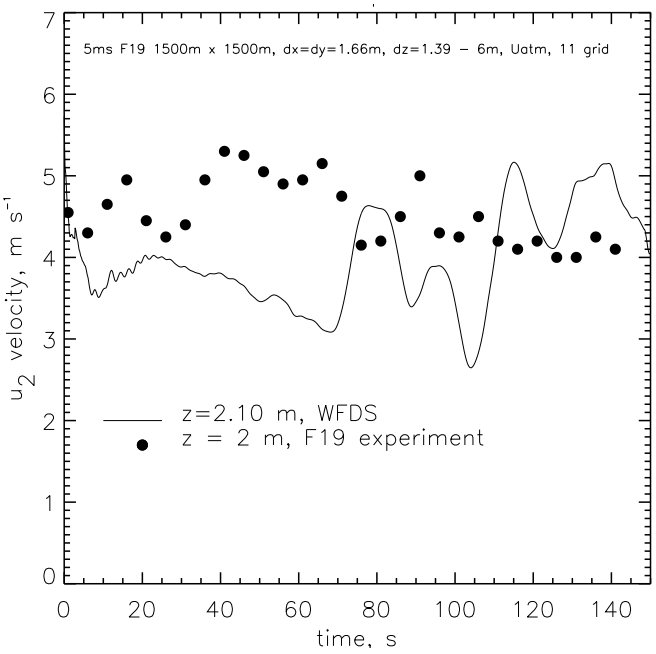

(a)

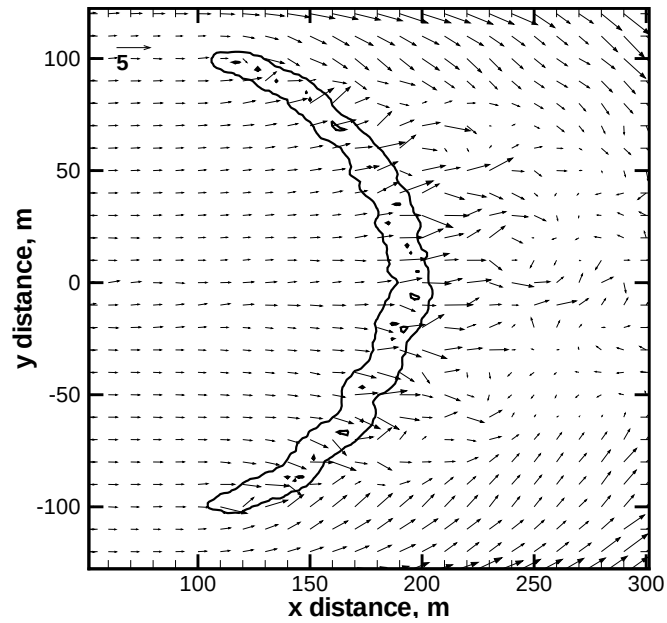

(b)

Figure 13: WFDS and experimental results for experiment F19 at $t = 100$ s. The ignition line fire was located at 50 m $\leq\ x\ \leq$ 53.3 m, -86.7 m $\leq\ y\ \leq$ 86.7 m **(a)** Time history of U_2. WFDS predictions averaged over 5 s (solid line) are located at a height of $z = 2.1$ m above the midpoint of the ignition line (point $x = 50$, $y = 0$ in figure (b)). Field measurements (filled circles) are the average of measurements taken every 5 s at $z = 2$ m at the upwind corners of the 200 m x 200 m grassland plot ($x = 50$ m, $y =$ -100 m, 100 m in figure (b)). **(b)** Velocity vectors at a height of 2.1 m from WFDS at time $t = 100$ s. Contour of the heat release rate showing borders of flaming region in the same plane is also shown. The WFDS grassland plot is located at $50\ \mathrm{m} \leq x \leq 250\ \mathrm{m},\ -100\ \mathrm{m} \leq y \leq 100\ \mathrm{m}$.

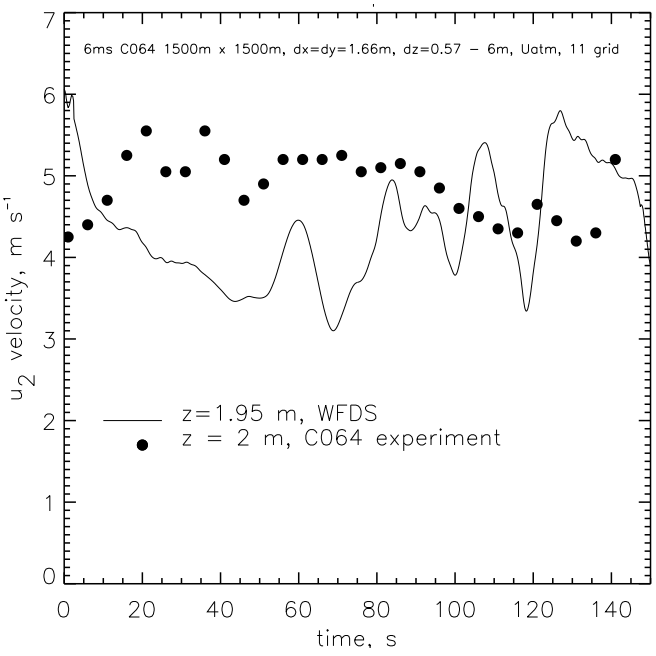

(a)

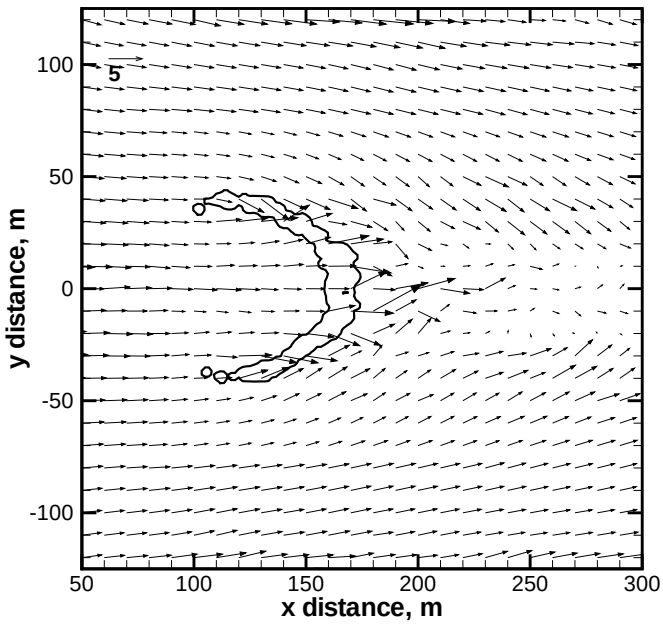

(b)

Figure 14: WFDS and experimental results for experiment C064 at $t = 75$ s. The ignition line fire was at 100 m $\leq \ x \ \leq =$ 101.6 m, -25 m $\leq \ y \ \leq$ 25 m. **(a)** Time history of U_2, the velocity 2 m above ground in the head fire spread direction. WFDS predictions averaged over 5 s (solid line) are located at a height of $z = 1.95$ m above the midpoint of the ignition line (point $x = 100$, $y = 0$ in figure (b)). Field measurements (filled circles) are the average of measurements taken every 5 s at $z = 1.95$ m at the upwind corners of the 104 m x 108 m grassland plot ($x = 100$, $y =$ -52, 52 in figure (b)). **(b)** Velocity vectors at a height of 1.95 m from WFDS at time $t = 100$ s. Contour of the heat release rate showing borders of flaming region in the same plane is also shown. The WFDS grassland plot is located at $100 \text{ m} \leq x \leq 202 \text{ m}, \ -53 \text{ m} \leq y \leq 53 \text{ m}$.

In this section, model predictions of fire perimeters from two experimental cases are presented. In the first experiment, called F19, the fuel is *Themeda* grass ($\sigma_s = 12240$ m^{-1}). The grassland plot is 200 m x 200 m and the ignition line fire is 175 m long. This line fire was created with drip torches carried by two field workers walking for 56 s (87.5 m) in opposite directions from the center point to the ends of the line fire. The average wind speed, measured at the corners of the grassland plot and not including measurements influenced by the fire, equaled 4.8 m s^{-1}. In the second experiment considered, called C064, the fuel is *Eriachne* grass ($\sigma_s = 9770$). This grass was cut to 50 % of its height with the cuttings removed. The grassland plot is 104 m x 108 m and the ignition line was 50 m long. The ignition line fire was created with drip torches carried by field workers walking in opposite directions for 26 s (25 m). The average wind speed was 4.6 m s^{-1}. Fuel bed characteristics are given in Table 1 for both experiments. WFDS simulates the ignition procedure by sequentially igniting strips of the fuel bed at a rate that matches the experimental procedure. An animation of the WFDS fireline and smoke plume for case F19 can be found at Mell et al. (2006).

The time history of U_2 from WFDS and experiment F19 and C064 are shown in Fig. 13(a) and Fig. 14(a), respectively. The experimental value of U_2 (filled circles) is the average of the magnitude of the velocity vector, averaged over 5 s, in the horizontal plane $z = 2$ m measured every five seconds at the two upwind corners of the grassland plot. The WFDS value of U_2 is the magnitude of the simulated velocity vector at the y midpoint of the ignition line fire and at a height of $z = 2.1$ m and $z = 1.95$ m for cases F19 and C064, respectively.

WFDS velocity vector components in the horizontal plane $z \cong 2$ m are shown in Fig. 13(b) and Fig. 14(b) for cases F19 and C064, respectively. Also shown is the outer boundary of the flaming region in the same plane, $z \cong 2$ m. Case F19 clearly has a larger fire perimeter. The F19 fireline also presents a greater blockage to the ambient wind as can be seen by the smaller vector lengths in Fig. 13(b), compared to Fig. 14(b), upwind of the head fire. Entrainment of air toward the fire from the far-field can be clearly seen.

Figures 15(a,b) contain the location of the leading edge of the head fire versus time, from both WFDS (solid line) and by using Eq. (2) (circles) for both experimental cases F19 and C064, respectively. The head width from WFDS is plotted as a dashed line. The head depth from both WFDS (dotted line) and its average value from the experiments (dash-dot line) are also shown. The average value of the WFDS head fire depths is 11.4 m for case F19 (experimental value was 10 m) and 12.2 m for case C064 (experimental value was 7.1 m). Overall, the spread rate of both cases agrees well with the empirical formula, Eq. (2). During the period of transient behavior in case F19, 76 s $\leq$ t $\leq$ 90 s in 15(a), the simulated flanking fires reach the boundaries of the grassland plot and extinguish. Before and after this period the simulated flame spread rate is nearly constant and in good agreement with Eq. (2).

The fire perimeters of cases F19 and C064 are shown in Figs. 16(a,b), respectively. The actively burning fire bed from WFDS is shown as shaded contours. The leading edge of the head fire from the experiments is plotted as symbols. In F19 a wind shift occurs in the experiment after $t = 86$ s which breaks the symmetry of the fire perimeter. This does not occur in WFDS since a constant wind orientation is assumed at the inflow boundary. As expected from the previous results, the spread of the head fire is well predicted at all times. The simulated fire reaches the downwind fire break at 133 s; the experimental fire at 138 s. Before the wind shift, the predicted fire perimeter closely matches the measured fire perimeter. After t = 86 s it is not clear how well WFDS predicts the entire fireline because the wind shift significantly changes the observed fire perimeter. Also, long flanking fires (as, for example, those shown in Fig. 9(c)) do not develop for this case because the flank fires reach the fire breaks relatively soon.

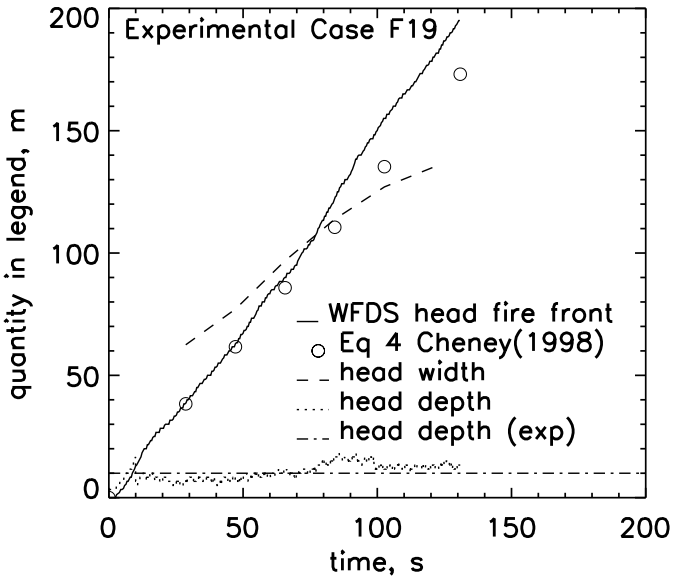

(a)

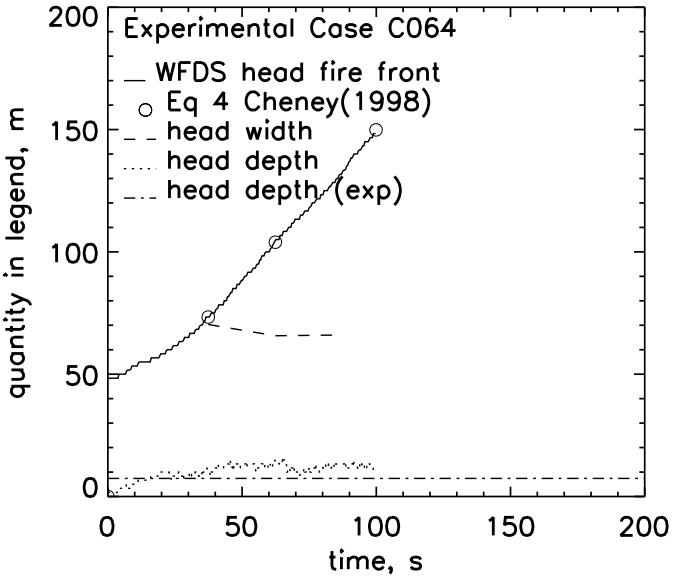

(b)

Figure 15: Time histories of the location of the leading edge, the width, and the depth of the head fire for experimental cases F19 and C064. The leading edge of the head fire from WFDS is shown as a solid line and as filled circles using the empirical spread rate formula, Eq. 2, with WFDS values for the head width, W. The head width from WFDS is a dashed line and the instantaneous depth a dotted line. The average head fire depth from field measurements is a dash-dot line.

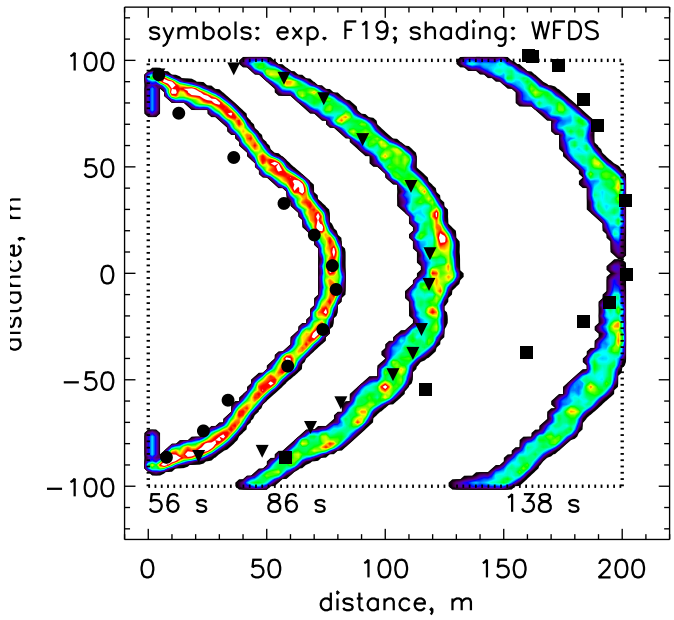

(a)

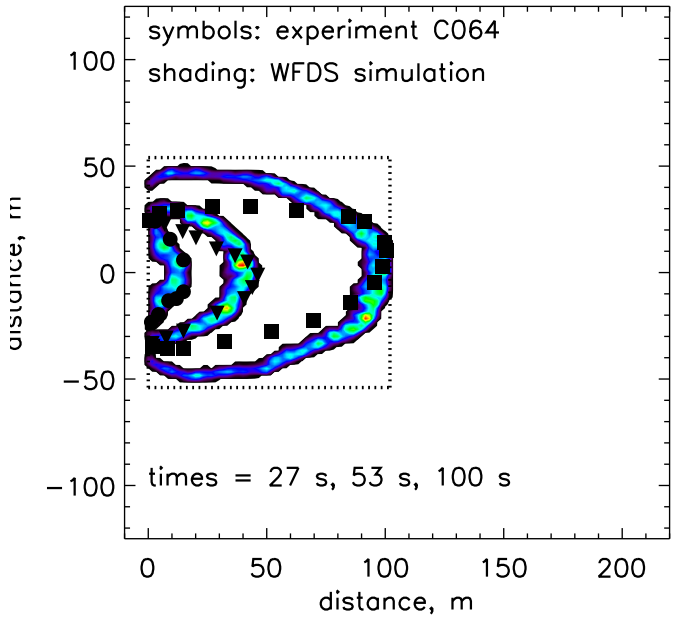

(b)

Figure 16: Shaded contours show the actively burning fire bed (nonzero mass flux of gaseous fuel) from WFDS; symbols show the leading edge of the observed fire front in the experiments. The borders of the grassland plot are represented by the dashed line. **(a)** experiment F19 and **(b)** is experiment C064. See text for details and Table 1 for fuel/environmental parameters.

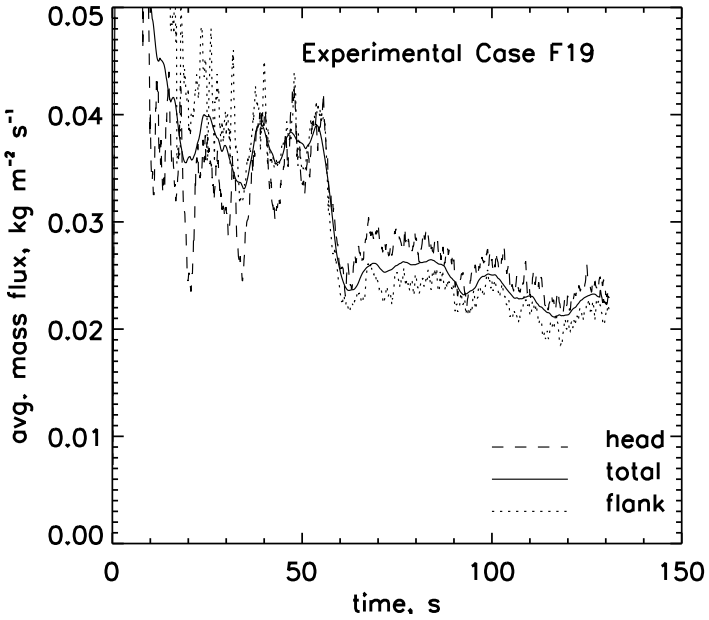

(a)

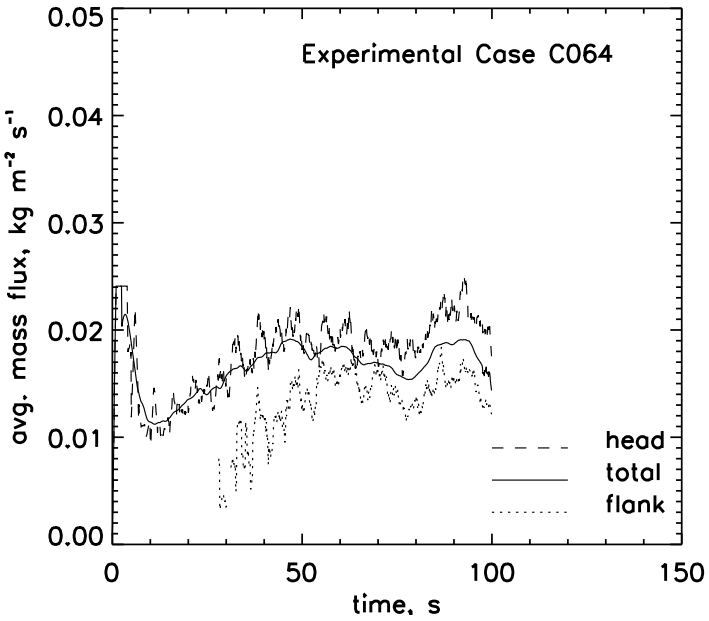

(b)

Figure 17: WFDS time histories, for experimental cases F19 and C064, of the mass flux of fuel gases during pyrolysis, $\dot{m}''_{\rm s,pyr}$ (kg m^{-2}s^{-1}), averaged over the head fire, flank fires, and the total fire perimeter. In both figures $L_{\rm ig} = 100$ m. **(a)** is experimental case F19 and **(b)** is experimental case C064.

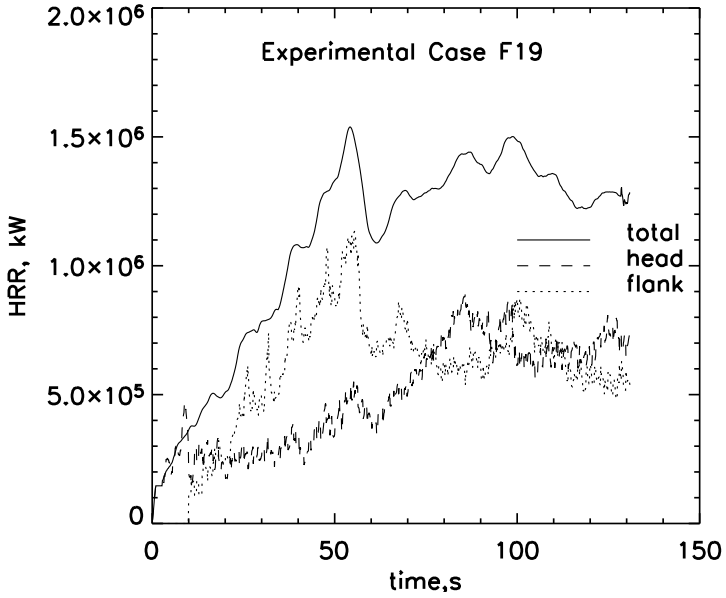

(a)

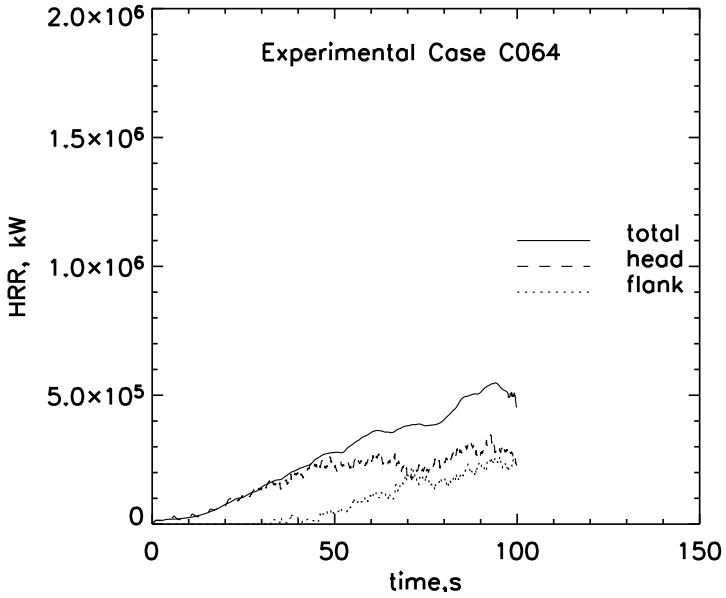

(b)

Figure 18: WFDS time histories, for experimental cases F19 and C064, of the heat release rate, HRR (kW), in the head fire, flank fires, and the total fire. **(a)** is experimental case F19 and **(b)** is experimental case C064.

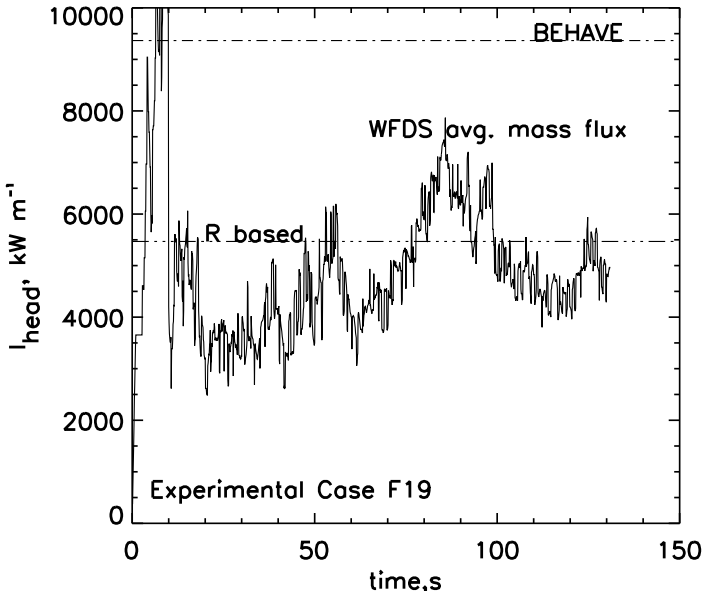

(a)

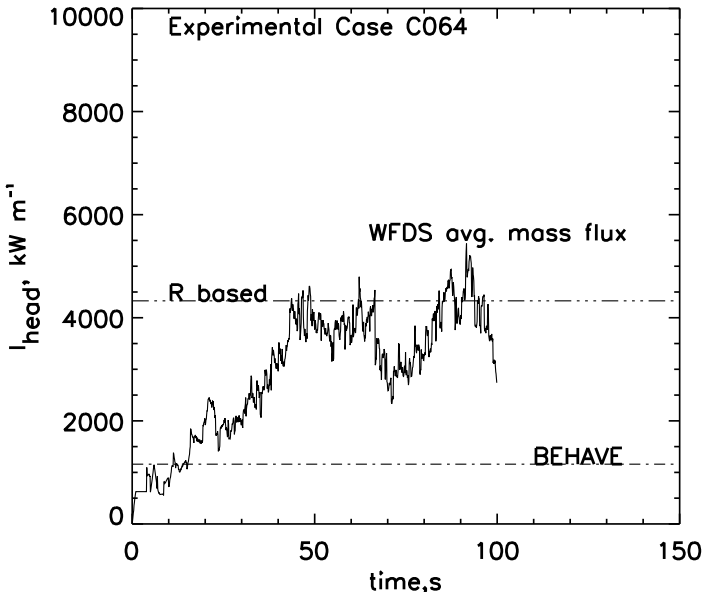

(b)

Figure 19: Time history, for experimental cases F19 and C064, of the fire line intensity, I (kW m^{-1}), in the head fire region of the fire perimeter. Solid line is from WFDS. The value of I from BehavePlus (line labelled 'BEHAVE') and from $I = \Delta h_{\rm c}(1-\chi_{\rm char})w_{\rm s}R$ using the experimentally measured R (line labelled 'R based'; see Eq. (6)) are also shown. **(a)** is experimental case F19 and **(b)** is experimental case C064.

In case C064, shown in Fig. 16(b) extended free burning flank fires do develop. The spread rate of the head fire is well predicted. WFDS over predicts the spread rate of the flank fires. The reasons for this are the subject of ongoing model development efforts. The current version of WFDS does not faithfully model the upward spread mechanism that can be present in flank fires. Instead, the fire burns downward through the grassland fuel bed everywhere along the perimeter. Also, flank fire depths in the field were observed to be significantly smaller than head fire depths. The horizontal grid resolutions used here (1.66 m) adequately resolve the head fire depth but this may not be the case for the flank fires.

Figures 17(a,b) are plots of the spatially averaged mass flux in the head and flank fire regions of the fire perimeter and the total perimeter for case F19 and C064, respectively. Case C064 has a smaller mass flux which is consistent with its smaller fuel load. The initial period of larger mass flux in F19 ($t < 60$ s) is due to the ignition line fire. The ignition procedure stops at $t = 56$ s. Figures 18(a,b) show the heat release rates associated with the entire fire perimeter and the head and flanking fires for both experimental cases. The HRR in case C064 is significantly smaller than F19 due to its lighter fuel loading and shorter fireline perimeter. In case F19, the flanking fires dominate the total HRR during the ignition phase. During the latter part of the F19 case HRR $\cong$ 1.4 GW (or $I_{\rm R} = 350$ kW m^{-2}). For comparison, estimates of $I_{\rm R}$ during the burning of logging slash are approximately $I_{\rm R} = 75$ kW m^{-2} (Ohlemiller and Corley 1994). The actively burning area in the logging slash fire was approximately 2 $\times 10^5$ m^2. This is 50 times larger than the actively burning area in the latter half of the F19 simulation. For this reason the total HRR in the logging slash fires was 15 GW, approximately 10 times larger than the F19 grassland fire.

The spatially averaged head fire mass flux in Figs. 17(a,b) is used in Eq. (5) to determine the time history of $I_{\rm R}$ for the head fire (not shown). The time history of I for the head fire is then determined from $I_{\rm R}$ and d by using Equation (6). The resulting head-fireline intensity is plotted (solid line) in Figs. 19(a,b) for case F19 and C064, respectively. Also plotted are the values of I determined from the experimentally observed head fire spread rates using the last relation on the right-hand-side of Eq. (6) (line labelled 'R based') and from the semi-empirical model BehavePlus (line labelled 'BEHAVE'). The experimentally observed head fire spread rates are $R = 1.4$ m s^{-1}, 1.2 m s^{-1} for F19 and C064, respectively. For these experimental conditions the simple approach using the head fire spread rate provided a better estimate of I than BehavePlus. The BehavePlus values were obtained by using the experimentally measured values of fuel load, moisture, surface-to-volume ratio, and fuel bed depth which are listed in Table 1, and the average of measured values for the moisture of extinction (22 %, Cheney et al. (1998)). The mid-flame wind speeds of 4.4 m s^{-1} for F19 and 2.8 m s^{-1} for C064 were used. The dead fuel heat content was 18608 kJ kg^{-1}, which is listed in NFFL descriptions for grass fuels UCSB (2005). BehavePlus predictions of the head-fireline intensity are nearly a factor of two too large for case F19 and a factor of four too small for case C064. This is due to BehavePlus over predicting the spread rate for F19 (R = 4.4 m s^{-1}) and under predicting it for C064 ($R = 0.47$ m s^{-1}). This is relevant to mesoscale coupled atmosphere-fire models currently under development (e.g., Clark et al. (2003, 2004) and Coen (2005)) since their heat and mass fluxes from the fire into the atmosphere are based in part on spread rate predictions from empirical and semi-empirical spread rate formulas. These results imply that, for AU grassland fuels, the empirical fire spread formula should be used rather than the semi-empirical (Rothermel 1972) spread rate.

5 Summary and Conclusions

A physics-based, transient, three–dimensional, coupled fire-atmosphere model for simulating fire spread through surface fuels on flat terrain, was developed and evaluated using observational data from Australian grassland fires. This model, called WFDS, is an extension, to vegetative fuels, of the structural Fire Dynamics Simulator (FDS) developed at the National Institute of Standards and Technology (NIST). Grassland fires were chosen here because of the simplicity of both the fuel and terrain, and because a significant amount of experimental data (for Australian grassland fires) exists for model validation.

Sixteen fires (four different ignition line lengths and four different wind speeds) were simulated. Head fire spread rates from WFDS were compared to an empirical relation developed from experimental data. Overall, WFDS predictions of the dependence of the head fire spread rate on both the ambient wind speed and on the head fire width were similar to an empirical relation.

Two specific Australian grassland experiments were also simulated. In both cases the location of the head fire was well predicted. One experimental case had extended, freely spreading, flank fires. WFDS over predicted the spread rate of these flank fires. The reasons for this are under investigation. One possibility is that flank fires are under resolved, since their fire depth can be significantly smaller than head fires. Some light may be shed on this issue by comparing to a larger number of experimental fires. We plan to extend the validation effort to a larger set of experiments and to a wider range of fuel parameters (moisture, surface to volume ratio, packing ratio) in order to better assess WFDS capabilities.

Areas for further model development and model evaluation include:

- The vegetation model is not appropriate for fuels through which significant vertical flame spread can occur. A model approach for suspended vegetation, such as tree crowns, has been implemented and is currently being evaluated. Preliminary results can found in Mell et al. (2006).

- The grassland fuel bed is assumed to burn from the top down. This is consistent with field observations of head fires, which spread with the ambient wind. It is not consistent with backing or flanking fire behavior, based on observations. This may play a role in the over prediction of flank fire spread rates.

- Char oxidation has not been considered. For this reason, smoldering or glowing combustion of the fuel after the fire front has passed is not present. This can be an important contribution to overall smoke generation.

- The underestimation of convective heat transfer into the solid fuel in regions of active combustion, and the sensitivity of the results to changes in how the drag and convective heat transfer is modeled needs further investigation.

- A more complete evaluation of the model's performance for a range of fuel and environmental parameters (e.g., moisture level, surface-to-volume ratios, bulk fuel loadings, wind speeds, and wind profiles) is required.

Multidimensional numerical fluid–dynamical wildfire simulation models can be used to study the behavior of wildfire and wildland-urban interface fires. However, depending on the scope of the physical models employed they can require computational resources that preclude real-time forecasts. Such is the case with the version of WFDS presented here. This model, therefore, has not been designed to replace operational models, but it can be used to expand or improve their capabilities.

The computational cost of physics-based wildland fire modeling limits the application of the approach to modeling wildfire behavior within a certain scale range. In models like WFDS, computational resources are devoted to resolving fire combustion and the close–in fire-atmosphere flow. In large-scale coupled atmosphere-wildfire models the thermal degradation of solid fuel is not modeled directly and combustion is parameterized. Empirical or semi-empirical models for fire spread rates and heat and mass fluxes from the fire to the atmosphere are used (Clark et al. 1996, 2003, 2004; Coen 2005). Computational resources can then be devoted to resolving the large scale fire-atmospheric physics.

Large scale fire-atmosphere interactions are considered to be of major importance to predicting fire behavior, especially severe fire behavior. A longer term goal, therefore, is to develop and test (using WFDS) improved models of fire physics suitable for use in large scale atmosphere-wildfire models. Once suitably validated, both the WFDS and a large scale coupled atmosphere–wildfire model can be used to evaluate operational models over a wide range of conditions and real–time applications, such as prediction of firebrand generation and transport, and fire spread rates. They can also be used to improve our understanding of how fuel conditions (amount, type, moisture content), terrain and weather are responsible for severe and blow-up fires.

Another long term goal at NIST is the development of a simulation tool for wildland-urban interface fires. The cost in insured damages from these fires can significantly outweigh the operational costs of fighting the fire. The fuels in these fires are an intermix of continuous and discrete vegetative fuels and structural materials. These fuel types, and their spatial arrangement, fall outside traditional wildland fuel classification methods and, therefore, current fire-risk assessment methods or models. A suitably validated simulation tool could be used to help determine and assess the important risk factors in existing and planned communities.

6 Acknowledgements

The first author would like to thank Dr. Ron Rehm of NIST for many fruitful discussions during the writing of this paper. This work was sponsored in part by the USDA Forest Service Joint Venture Agreement 03-JV-11231300-088.

References

F.A. Albini. A model for fire spread in wildland fuels by radiation. *Combust. Sci. and Tech.*, 42: 229–258, 1985.

F.A. Albini. Wildland fire spread by radiation – a model including fuel cooling by natural convection. *Combust. Sci. and Tech.*, 45:101–113, 1986.

F.A. Albini. *Fire in the Environment: The Ecological, Atmospheric, and Climatic Importance of Vegetation Fires*, chapter 3. Dynamics and modeling of vegetation fires: Observations. John Wiley and Sons, 1993.

F.A. Albini. Estimating wildfire behavior and effects. Technical Report USDA For. Serv. Gen. Tech. Rep. INT–30, USDA Forest Service, 1976.

H.E. Anderson. Heat transfer and fire spread. Technical Report USDA For. Serv. Res. Pap. INT-69, USDA Forest Service, 1969.

P.L. Andrews. BEHAVE: Fire behavior prediction and modeling system – BURN subsystem part 1. Technical Report USDA For. Serv. Gen. Tech. Rep. INT-194, USDA Forest Service, 1986. 130 pp. program available at http://fire.org.

P.L. Andrews, C. D. Bevins, and R. C. Seli. BehavePlus fire modeling system, version 2.0: User's Guide. Technical Report USDA For. Serv. Gen. Tech. Rep. RMRS-GTR-106WWW, USDA Forest Service, 2003. 132 pp. program available at http://fire.org.

M. Appicello. Policy implications of large fire management, 2006. http://www.fs.fed.us/fire/management/Large_Fire_Mgt.pdf (verified 11/12/06).

A. Atreya. *Pyrolysis, ignition and fire spread on horizontal surfaces of wood.* PhD thesis, Harvard University, 1983.

C.P. Bankston, B.T. Zinn, R.F. Browner, and E.A. Powell. Aspects of the mechanisms of smoke generation by burning materials. *Combustion and Flame*, 41:273–292, 1981.

H.R. Baum and W.E. Mell. A radiative transport model for large-eddy fire simulations. *Combust. Theory Modelling*, 2:405–422, 1998.

T. Beer. The interaction of wind and fire. *Boundary-Layer Meteorology*, 54:287–308, 1991.

J.B. Bell, N.J. Brown, M.S. Day, M. Frenklach, J.F. Grcar, and S.R Tonse. The Dependence of Chemistry on the Inlet Equivalence Ratio in Vortex-Flame Interactions. *Proc. Combustion Inst.*, 28:1933–1939, 2000.

R.W. Bilger. *Turbulent Reacting Flows*, chapter 4. Turbulent Flows with Nonpremixed Reactants. Springer–Verlag, 1980.

USFS BlueSky. Bluesky modeling framework to predict cumulative impacts of smoke from agricultural, forest, and range fires, 2004. http://www.airfire.org/bluesky/.

B.W. Butler. . In *Proceedings: 12th Conference of Fire and Forest Meteorology*, 1993. p. 26.

C. Chandler, P. Cheney, L. Thomas, P. Trabaud, and D. Williams. *Fire in Forestry.* John Wiley & Sons, 1983. Chapter 1: Chemistry and physics of ignition and combustion; pp. 1-30.

N.P. Cheney and J.S. Gould. Fire growth in grassland fuels. *Int. J. of Wildland Fire*, 5(4):237–247, 1995.

N.P. Cheney, J.S. Gould, and W.R. Catchpole. The influence of fuel, weather and fire shape variables on fire spread in grasslands. *Int. J. of Wildland Fire*, 3(1):31–44, 1993.

N.P. Cheney, J.S. Gould, and W.R. Catchpole. Prediction of fire spread in grasslands. *Int. J. of Wildland Fire*, 9(1):1–13, 1998.

T.L. Clark, M.A. Jenkins, J. Coen, and D. Packham. A coupled atmospheric-fire model: Convective feedback on fire-line dynamics. *J. Applied Meteorology*, 35:875–901, 1996.

T.L. Clark, M. Griffiths, M.J. Reeder, and D. Latham. Numerical simulations of grassland fire in the Northern Territory, Australia: A new subgrid-scale fire parameterization. *J. of Geophysical Res.*, 108(D18):doi: 10.1029/2002JD003340. issn: 0148–0227, 2003.

T.L. Clark, J.L. Coen, and D. Latham. Description of a coupled atmosphere-fire model. *Intl. J. Wildland Fire*, 13(1):49–63, 2004.

J. Coen. Simulation of the Big Elk Fire using coupled atmosphere-fire modeling. *Infl. J. Wildland Fire*, 14:49–59, 2005.

J.L. Coen. Simulation of wildfire incidents using coupled atmosphere-fire modeling. In *Second International Wildland Fire Ecology and Fire Management Congress and Fifth Symposium of Fire on Forest Meteorology*. American Meteorological Society, 2003. paper J2.4, Available at http://ams.confex.com/ams/pdfpapers/65709.pdf [Verified 18 October 2006].

J.J. Colman and R.R. Linn. Non-local chemistry implementation in HIGRAD/FIRETEC. 2003.

J.J. Colman and R.R. Linn. Separting combustion from pyrolysis in HIGRAD/FIRETEC. 2005.

A.M. Costa, J.C.F. Pereira, and M. Siqueira. Numerical prediction of fire spread over vegetation in arbitrary 3D terrain. *Fire and Materials*, 19:265–273, 1995.

K.P. Davis. *Forest Fire: Control and Use*. McGraw-Hill, New York, 1959.

N.J. De Mestre, E.A. Catchpole, D.H. Anderson, and R.C. Rothermel. Uniform propagation of a planar fire front without wind. *Combust. Sci. and Tech.*, 65:231–244, 1989.

C. Di Blasi. Modeling and simulation of combustion processes of charring and non-charring solid fuels. *Prog. Energy Combust. Sci.*, 19:71–104, 1993.

A.P. Dimitrakipoulos. . *J. Anal. Appl. Pyol.*, 60:123, 2001.

J.L. Dupuy and D. Morvan. Numerical study of the a crown fire spreading toward a fuel break using a multiphase physical model. *International Journal of Wildland Fire*, 14:141–151, 2005.

M.A. Finney. FARSITE: Fire Area Simualtor-Model, Development and Evaluation. Technical Report RMRS-RP-4, USDA Forest Service, Rocky Mountain Research Station Paper, 1998.

W.L. Fons. Analysis of fire spread in light forest fuels. *J. Agricultural Research*, 72(3):93–121, 1946.

G.P. Forney and K.B. McGrattan. User's Guide for Smokeview Version 4: A Tool for Visualizing Fire Dynamics Simulation Data. Technical Report NISTIR Special Publication, 1017, National Institute of Standards and Technology, Gaithersburg, Maryland, August 2004. http://www.fire.nist.gov/fds/docs/sv_users_guide_4.pdf.

GAO. Technology Assessment: Protecting Structures and Improving Communications during Wildland Fires. Technical Report GAO-05-380, United State Government Accountability Office, April 2005. Report to Congressional Requestors.

GAO. Western national forests: A cohesive strategy is need to address catastrophic wildfire threats. Technical Report GAO/RCED-99-65, Committee on Resources, House of Representatives, April 1999. Report to the Subcommittee on Forests and Forest Health.

J.S. Gould. Validation of the Rothermel fire spread model and related fuel parameters in grasslands fuels. CSIRO, Canberra, ACT, July 11-12 1988.

A.M Grishin. *Fire in Ecosystems of Boreal Eurasia*, chapter Chapeter 6. Mathematical modelling of forest fires. Kluwer Academic Publishers, Dordrecht, The Netherlands, 1996. pp. 314–325.

A.M. Grishin, A.D. Gruzin, and V.D. Zverev. Study of the structure and limits of propagation of the front of an upstream forest fire. *Combustion, Explosion, and Shock Waves*, 21(1):9–18, 1985.

K.G. Hirsch. Canadian forest fire behavior prediction (FBP) system: user's guide. Technical Report Special Report 7, Canadian Forest Service, Northwest Region, Northern Forestry Centre, 1996. 122 pp.

J.P. Holman. *Heat Transfer*. McGraw–Hill, New York, 5th edition, 1981. page 285.

W.Q. Hough. Caloric value of some forest fuels of the southern United States. Technical Report USDA Foerst Service Research Note SE-120, Southeastern Forest Experiment Station, Southeastern Forest Experiment Station, Ashville, North Carolina, US Dept. of Agriculture, Forest Service, 1969. 6 pp.; http://www.srs.fs.usda.gov/pubs.

F.P. Incropera and D.P. Dewitt. *Fundamentals of Heat and Mass Transfer*. John Wiley & Sons, New York, 4th edition, 1996. page 846.

P.G. Jarvis, G.B. James, and J.J. Lansberg. *Vegetation and the Atmosphere, Vol. 2 case studies*, chapter 7. Coniferous Forest, pages 172–240. Academic Press, New York, 1976.

E.A. Johnson and K. Miayanishi, editors. *Forest Fires: Behavior and Ecological Effects*. Academic Press, 2001.

H. Koseki and G.W. Mulhooand. The effect of diameter of the burning of crude oil pool fires. *Fire Technology*, 54, 1991.

M. Larini, F. Giroud, B. Porterie, and J.-C. Loraud. A multiphase formulation for fire propagation in heterogeneous combustible media. *Int. J. Heat Mass Transfer*, 41:881–897, 1998.

R. Linn and P. Cunningham. Numerical simulations of grass fires using a coupled atmosphere-fire model: Basic fire behavior and dependence on wind speed. *J. Geophysical Res.*, 110, 2005.

R. Linn, J. Reisner, J.J. Colman, and J. Winterkamp. Studying wildfire behavior using FIRETEC. *Intnl. J. of Wildland Fire*, 11:233–246, 2002.

R.R. Linn. personal communication, 2005.

R.R. Linn. *A transport model for prediction of wildfire behavior*. PhD thesis, New Mexico State University, 1997. also published as Los Alamos Report, LA-13334-T, 1997.

J. Margeri and O Sero-Guillaume. Modelling forest fires: Part II: reduction to two-dimensional models and simulation of propagation. *Intl. J. Heat and Mass Transfer*, 45:1723–1737, 2002.

K.B. McGrattan. Fire Dynamics Simulator (Version 4), Technical Reference Guide. Editor, McGrattan, K.B. NISTIR Special Publication, 1018, National Institute of Standards and Technology, Gaithersburg, Maryland, September 2005. http://www.fire.nist.gov/fds/docs/fds_tech_guide_4.pdf.

W. Mell, A. Maranghides, R. Rehm, S. Manzello, G. Forney, M.A. Jenkins, R. Sun, and S. Krueger. url for nist's wildland-urban interface fire webpage, 2006. http://http://www2.bfrl.nist.gov/userpages/wmell/public.html.

W.E. Mell and J.R. Lawson. A Heat Trasfer Model for Firefighters' Proctective Clothing. *Fire Technology*, 36:39–68, 2000.

W.E. Mell, K.G. McGrattan, and H.R. Baum. Numerical simulation of combustion in fire plumes. *Proc. Combustion Inst.*, 26:1523–1530, 1996.

W.E. Mell, S.L. Olson, and T. Kashiwagi. Flame spread along free edges of thermally thin samples in microgravity. *Proc. Combust. Inst.*, 28:473–479, 2000.

W.E. Mell, J.J. Charney, M.A. Jenkins, P. Cheney, and J. Gould. Numerical simulations of grassland fire behavior from the LANL-FIRETEC and NIST-WFDS models. EastFIRE Conference, May 11–13 2005. George Mason University, Fairfax, VA.

C. Moro. Technical Report. Technical report, INRA Equipe de Pré des Incendies de Forêt, 1997.

D. Morvan and J.L. Dupuy. Modeling Fire Spread Through a Forest Fuel Bed Using a Multiphase Formulation. *Comb. Flame*, 127:1981–1984, 2001.

D. Morvan and J.L. Dupuy. Modeling the propagation of a wildfire through a Mediterrean shrub using a multiphase formulation. *Comb. Flame*, 138:199–210, 2004.

D. Morvan, V. Tauleigne, and J.L. Dupuy. Wind Effects on Wildfire Propagation Through a Mediterranean Shrub. Millpress, Rotterdam, ISBN 90-77017-72-0, 2002a. also Communications from Fire Star consortiums members at the IV International Conference on Forest Fire Research, Luso, November 18-21, 2002.

D. Morvan, V. Tauleigne, and J.L. Dupuy. Flame Geometry and Surface to Crown Fire Transition During the Propagation of a Line Fire Through a Mediterranean Shrub. Millpress, Rotterdam, ISBN 90-77017-72-0, 2002b. also Communications from Fire Star consortiums members at the IV International Conference on Forest Fire Research, Luso, November 18-21, 2002.

P.J. Murphy, J.P. Mudds, B.J. Stocks, E.S. Kasischke, D. Barry, M.E. Alexander, and N.H.F French. *Ecological Studies, Vol. 138, Fire, climate change, and carbon cycling in the boreal forest*, chapter Historical fire records in the North American boreal forest, pages 274–288. Springer-Verlag, New York, New York, USA, 2000.

NAS. *A Study of Fire Problems*, chapter Appendix IV: Note on radiative transport problems arising in fire spread. National Academy of Sciences – National Research Council, Washington, D.C., 1961. Publication 949.

I.R. Nobel, G.A.V. Bary, and A.M. Gill. McArthur's fire-danger meters expressed as equations. *Australian J. of Ecology*, 5:201–203, 1980.

T. Ohlemiller and D. Corley. Heat release rate and induced wind field in a large scale fire. *Combust. Sci. Tech.*, 97:315–330, 1994.

M.N. Ozisk. *Radiative Heat Transfer and Interactions with Conduction and Convection.* John Wiley & Sons, 1st edition, 1973.

P.J. Pagni and T.G. Peterson. Fire spread through pourous fuels. *Proc. Combust. Inst.*, 14:1099–1107, 1973.

W.J. Parker. Prediction of the heat release rate of douglas fir. pages 337–346. International Association for Fire Safety Science, June 13-17 1988. Hemisphere Publishing, New York.

E. Pastor, L. Zarate, E. Planas, and J Arnaldos. Mathematical models and calculations systems for the study of wildland fire behavior. *Prog. Energy. Combust. Sci.*, 29:139–153, 2003.

W.M. Pitts. Wind effects on fires. *Prog. Energy. Combust. Sci.*, 17:83–134, 1991.

B Porterie, D. Morvan, M. Larini, and J.C. Loraud. Wildfire propagation: a two-dimensional multiphase approach. *Combust. Explos. Shock Waves*, 34:139–150, 1998. also in Fizika Goreniya i Vzryva, Vol. 34, p.26, (1998).

B Porterie, D. Morvan, J.C. Loraud, and M. Larini. Firespread through fuel beds: Modeling of wind-aided fires and induced hydrodynamics. *Phys. Fluids*, 12(7):1762–1782, 2000.

J.G. Quintiere. *Principles of Fire Behavior*. Delmar Publishers, Albany, 1997.

G.D. Raithby and E.H. Chui. A Finite-Volume Method for Predicting Radiant Heat Transfer in Enclosures with Participating Media. *J. Heat Transfer*, 112(2):415–423, 1990.

R.G. Rehm and H.R. Baum. The Equations of Motion for Thermally Driven, Buoyant Flows. *Journal of Research of the NBS*, 83:297–308, 1978.

J. Reisner, S. Wynne, L. Margolin, and R. Linn. Coupled Atmosphere-Fire Modeling Employing the Method of Averages. *Monthly Weather Review*, 128:3683–3691, 2000.

S.J. Ritchie, K.D. Steckler, A. Hamins, T.G. Cleary, J.C. Yang, and T. Kashiwagi. The effect of sample size on the heat release rate of charring materials. pages 177–188. International Association for Fire Safety Science, March 3–7 1997.

D.E. Rosner. *Transport Processes in Chemically Reacting Flow Systems*. Dover Publications, Inc., Mineola, New York, 2000.

R.C. Rothermel. A mathematical model for predicting fire spread in wildland fuels. Technical report, 1972.

O. Sero-Guillaume and J. Margeri. Modelling forest fires: Part I: a complete set of equations derived by extended irreversible thermodynamics. *Intl. J. Heat and Mass Transfer*, 45:1705–1722, 2002.

J. Smagorinksy. General Circulation Experiments with the Primitive Equations I. The Basic Experiment. *Monthly Weather Review*, 91:99–164, 1963.

R.J. Sneeuwjagt and W.H. Frandsen. Behavior of experimental grass fires vs. predictions based on Rothermel's fire model. *Can. J. For. Res.*, 7:357–367, 1977.

G.L. Stephens. The parameterization of radiation for numerical weather prediction and climate models. *Monthly Weather Review*, 112:827–867, 1984.

S. Stewart, V. Radeloff, and Hammer R. Characteristics and location of the wildland-urban interface in the United States. Novemeber 19, Orlando, FL 2003. http://ams.confex.com/ams/pdfpapers/65316.pdf.

B.J. Stock and A.J. Simard. Forest Fire Management in Canada. *Disaster Managment*, 5(1):21–27, 1993.

R.A. Susott. Characterization of the thermal properties of forest fuels by combustible gas analysis. *Forest Sci.*, 2:404–420, 1982.

UCSB. University of southern california, santa barbara: Southern california wildfire hazard center, 2005. http://www.icess.ucsb.edu/resac/.

R.O. Weber. Modelling fire spread through fuel beds. *Prog. Energy Combust. Sci.*, 17:67–82, 1991.

A.L Westerling, H.G. Hidalgo, D.R. Cayan, and T.W. Swetnam. Warming and earlier spring increases western U.S. forest wildfire activity. *Science*, 313:940–943, 2006.

F.A. Williams. Urban and wildfire fire phenomenology. *Prog. Energy Combust. Sci.*, 8:317–354, 1982.

R. Yuen, R. Casey, G. De Vahl Davis, E. Leonardi, G.H. Yeoh, V. Chandrasekaran, and S.J. Grubits. A three-dimensional mathematical model for the pyrolysis of wet wood. pages 189–200. Intnl. Assoc. for Fire Safety Science, March 3–7 1997.

X.Y. Zhou and J.C.F. Pereira. A multidimensional model for simulating vegetation fire spread using a porous media sub-model. *Fire and Materials*, 24:37–43, 2000.

J. Zicherman. Fire at the urban wildland interface: Performance of California homes and buildings. Technical Report IFB No: 5CA334189 FCA No.: 05-6369, Fire Cause Analysis, Richmond, CA, 2004. prepared for California Dept. Forestry and Fire Protection, Rodney Slaughter.

A Model equations

A.1 Approach for modeling the gas phase

The governing equations for low Mach number flow with combustion are based on those derived in Rehm and Baum (1978), where it is assumed that pressure changes due to the fire or buoyancy induced flow are a small fraction of the ambient pressure (i.e., the pressure in the absence of the fire). The resulting equations are commonly known as a low Mach number approximation. Explicit second order Runge-Kutta time stepping and second order spatial differencing on a rectilinear grid is used. Additional details, especially of the numerical approach and boundary condition implementation can be found in McGrattan (2005). Ideal gases and Fickian diffusion are assumed. The equation for conservation of total mass is

$$\frac{\partial \rho}{\partial t} + \boldsymbol{u} \cdot \nabla \rho = -\rho \nabla \cdot \boldsymbol{u}. \tag{8}$$

This equation requires the divergence of the velocity $\nabla \cdot \boldsymbol{u}$. The determination of $\nabla \cdot \boldsymbol{u}$ is discussed in Sec. A.1.1.

The equation for conservation of momentum is

$$\frac{\partial \boldsymbol{u}}{\partial t} + \nabla \mathcal{H} - \boldsymbol{u} \times \boldsymbol{\omega} = \frac{1}{\rho}\left[(\rho - \rho_\infty)\boldsymbol{g} + \nabla \cdot \boldsymbol{\tau} - \boldsymbol{F}_{\mathrm{D}}\right], \tag{9}$$

$$\nabla \mathcal{H} = \frac{1}{2}\nabla |\boldsymbol{u}|^2 + \frac{1}{\rho}\nabla p_{\mathrm{d}} \cong \frac{1}{2}\nabla |\boldsymbol{u}|^2 + \frac{1}{\rho_\infty}\nabla p_{\mathrm{d}}, \tag{10}$$

$$\boldsymbol{\tau} = \mu_{\mathrm{LES}}\left(\mathrm{def}\ \boldsymbol{u} - \frac{2}{3}(\nabla \cdot \boldsymbol{u})\mathbf{I}\right). \tag{11}$$

Here the vector identity $(\boldsymbol{u}\cdot\nabla)\boldsymbol{u} = (1/2)\nabla|\boldsymbol{u}|^2 - \boldsymbol{u}\times\boldsymbol{\omega}$ is used and the deformation, or rate of strain, tensor is $\mathrm{def}\ \boldsymbol{u} = 0.5(\nabla \boldsymbol{u} + (\nabla \boldsymbol{u})^{\mathrm{T}})$. Equation (10) implies that $(1/\rho - 1/\rho_\infty)\nabla p_{\mathrm{d}}$ is negligible. Physically this amounts to assuming that the baroclinic torque has a negligible contribution, relative to buoyancy, to the generation of vorticity. With this assumption a constant coefficient PDE for the

pressure is formed by taking the divergence of the momentum equation [Eq.(9)]. This pressure PDE is solved in a computationally efficient and accurate manner using a direct solver. The baroclinic torque is then approximately restored using the pressure from the previous time step (McGrattan 2005).

The influence of the grass fuel bed on the ambient wind flow is approximated by the drag term $\boldsymbol{F}_{\rm D}$ in Eq. (9). This drag term is present only in the first gas-phase grid cell above the bottom boundary, and is determined by

$$\boldsymbol{F}_{\rm D} = \begin{cases} C_{\rm D}\frac{3}{8}\beta_{\rm s}\sigma_{\rm s}\rho|\boldsymbol{u}|\boldsymbol{u}\left[1-0.9\ m^{\rm f}_{\rm s,pyr}(t)\right], & 0 \le m^{\rm f}_{\rm s,pyr} < 1, \\ C_{\rm D}\frac{3}{8}\beta_{\rm s}\sigma_{\rm s}\rho|\boldsymbol{u}|\boldsymbol{u}\ [0.1], & m^{\rm f}_{\rm s,pyr} = 1, \end{cases} \tag{12}$$

where $C_{\rm D} \equiv 1$ is used which approximates a grass fuel element as a cylinder; $\beta_{\rm s}$ is the packing ratio of the solid fuel, $\sigma_{\rm s}$ is the surface to volume ratio of the solid fuel particles, and

$$m^{\rm f}_{\rm s,pyr}(t) = \frac{\int_0^t \dot{m}''_{\rm s,pyr}(t')dt'}{m''_{\rm s}(0)(1-\chi_{\rm char})}. \tag{13}$$

Here $\dot{m}''_{\rm s,pyr}$ is the rate of fuel gas generation due to pyrolysis of the vegetative solid, $m''_{\rm s}$ is the mass loading (mass per unit area) of the solid fuel bed, and $\chi_{\rm char}$ is the char fraction of the solid fuel. Equation (13) is the fraction of fuel that has undergone pyrolysis. Similar expressions for the terms not in the square brackets of Eq. (12) are used by Porterie et al. (2000) and Linn et al. (2002). The term in the square brackets approximates the weakening drag of the grass on the air flow as it burns away. For a given gas density and velocity field the drag of the fuel bed is reduced to 10% of its original value at the end of burning. The vegetative fuel variables in Eq. (12) are discussed more fully in Sec. A.2. This is a simple, first–step, model for representing the drag of the fuel bed. This approach is more explicit than the traditional boundary-layer meteorology method of treating the fuel as a zero-depth, constant friction surface of a particular roughness length based on the wind. It has the advantage of simplicity, a direct relationship to commonly measured fuel properties that are used in the fuel model, and varies with fuel consumption. How well it captures the influence of drag over a range of conditions is the subject of future research.

The computational grids used for the large fire simulations conducted here are too coarse to capture molecular transport physics. Instead an approximation to these subgrid processes using quantities resolved on the computational grid must be made. One approach to doing this is called called large eddy simulations (LES), a variant of which is used here. Following Smagorinksy (1963) a subgrid scale model for the dynamic viscosity in the viscous stress tensor is used, where

$$\mu_{\rm LES} = \rho(C\Delta)^2\left(2(\text{def }\boldsymbol{u})\cdot(\text{def }\boldsymbol{u}) - \frac{2}{3}(\nabla\cdot\boldsymbol{u})^2\right)^{\frac{1}{2}}. \tag{14}$$

Here C is an empirical constant (Smagorinsky constant), Δ is a length on the order of the grid cell size, and the deformation term is related to the dissipation function (the rate at which kinetic energy is converted to thermal energy). The thermal conductivity and material diffusivity are related to turbulent viscosity $\mu_{\rm LES}$ by

$$\lambda_{\rm LES} = \frac{\mu_{\rm LES}c_{\rm p,N_2}}{\rm Pr} \quad \text{and} \quad (\rho D)_{\rm LES} = \frac{\mu_{\rm LES}}{\rm Sc}. \tag{15}$$

The Prandtl and Schmidt numbers, Pr and Sc, are constant. Values of C, Pr, and Sc were obtained by comparing numerical simulations and laboratory experiments $C = 0.2$, $\rm Pr = Sc = 0.5$ (McGrattan

2005). The equation for the conservation of species is

$$\rho\frac{\partial Y_i}{\partial t}+\rho\boldsymbol{u}\cdot\nabla Y_i=\nabla\cdot\{(\rho D)_{\rm LES}\nabla Y_i\}+\dot m_i'''. \tag{16}$$

The equation of state is

$$p_o=\mathcal{R}\rho T\sum_i Y_i/M_i=\mathcal{R}\rho T/M. \tag{17}$$

The equation for conservation of energy is

$$\rho\frac{\partial h}{\partial t}+\rho\boldsymbol{u}\cdot\nabla h=\nabla\cdot(\lambda_{\rm LES}\nabla T)+\nabla\cdot\left(\sum_i h_i(\rho D)_{\rm LES}\nabla Y_i\right)-\nabla\cdot\dot{\boldsymbol{q}}_{\rm r}''+\frac{dp_o}{dt}. \tag{18}$$

Note that the WFDS simulations conducted here are not in a sealed enclosure, and therefore $dp_o/dt=0$. The energy release associated with chemical reactions is not explicitly present but is accounted for by h (Rosner (2000), see their Eq.[20]). Here

$$h(\boldsymbol{x},t)=\sum_i Y_i(\boldsymbol{x},t)h_i(T)\quad\text{ and }\quad h_i(T)=h_i^o+\int_{T^o}^{T}c_{{\rm p},i}(T')dT' \tag{19}$$

are the enthalpy of the mixture and of species i, respectively. The temperature only dependence of the enthalpy of ideal gases is used. Note that $c_{\rm p}=\sum_i Y_i dh_i/dT$ is the mixture specific heat.

The molar heat of combustion for a given chemical reaction at constant pressure is

$$\Delta\bar h_{\rm c}=-\sum_i\nu_i\bar h_i(T)=-\sum_i\nu_i h_i(T)M_i. \tag{20}$$

The simplified stoichiometric relation

$$\mathrm{C_{3.4}H_{6.2}O_{2.5}}+3.7\ (\mathrm{O_2}+3.76\ \mathrm{N_2})\rightarrow 3.4\ \mathrm{CO_2}+3.1\ \mathrm{H_2O}+13.91\ \mathrm{N_2} \tag{21}$$

is used to model the chemical reaction of air and fuel gases generated by wood pyrolysis (Ritchie et al. 1997). The mass consumption rate term for any of the species (except N_2 which is chemically inactive) can be written in terms of a specific one. Thus in terms of the fuel mass consumption rate,

$$\dot m_i'''=r_i\dot m_{\rm F}''',\ r_i=\frac{(\nu M)_i}{(\nu M)_{\rm F}},\quad \nu_{\rm F}=-1,\ \nu_{\rm O_2}=-3.7,\ \nu_{\rm CO_2}=3.4,\ \nu_{\rm H_2O}=3.1. \tag{22}$$

With this expression the heat release per unit volume rate of the combustion process can be represented in terms of the heat of combustion:

$$\dot Q_{\rm c}'''=-\sum_i h_i\dot m_i'''=-\frac{\dot m_{\rm F}'''}{(\nu M)_{\rm F}}\sum_i\nu_i h_i M_i=\frac{\dot m_{\rm F}'''}{(\nu M)_{\rm F}}\Delta\bar h_{\rm c}=-\dot m_{\rm F}'''\Delta h_{\rm c}. \tag{23}$$

Here $\Delta h_{\rm c}=\Delta\bar h_{\rm c}/M_{\rm F}$ is the mass based heat of combustion and the fact that $\nu_{\rm F}\equiv-1$ is used.

A.1.1 Divergence constraint

The divergence of the velocity is required in the conservation equation for total mass, Eq. (8). A general divergence constraint on the velocity can be derived by taking the material (or Lagrangian) derivative of the equation of state

$$\dot{p}_o = \frac{\mathcal{R}T}{M}\frac{D\rho}{Dt} + \frac{\mathcal{R}\rho}{M}\frac{DT}{Dt} + \mathcal{R}\rho T\sum_i \frac{1}{M_i}\frac{DY_i}{Dt} \tag{24}$$

and using Eqs. (8), (16), DT/Dt from Dh/Dt where h is expressed in Eq. (19), and Eq. (18):

$$\begin{aligned}\nabla\cdot\boldsymbol{u} &= \frac{1}{\rho c_\mathrm{p}T}\left(\nabla\cdot(\lambda_\mathrm{LES}\nabla T) + \sum_i (\rho D)_\mathrm{LES}\nabla Y_i\cdot\nabla h_i - \nabla\cdot\dot{\boldsymbol{q}}''_\mathrm{r}\right)\\ &\quad + \frac{1}{\rho}\sum_i \frac{M}{M_i}\nabla\cdot\{(\rho D)_\mathrm{LES}\nabla Y_i\} + \frac{1}{\rho}\sum_i\left(\frac{M}{M_i} - \frac{h_i}{c_\mathrm{p}T}\right)\dot{m}'''_i.\end{aligned} \tag{25}$$

A similar expression for the divergence constraint was used in simulations by Bell et al. (2000) of vortex flame interaction neglecting thermal radiation. Equation (25) can be simplified using the assumption that the ratio of specific heats, γ, for each species is equal to the value for diatomic gases, or

$$\gamma_i = \frac{\bar{c}_{\mathrm{p},i}}{\bar{c}_{\mathrm{v},i}} = \frac{c_{\mathrm{p},i}}{c_{\mathrm{v},i}} = \gamma = 7/5 \quad \Rightarrow\ \bar{c}_{\mathrm{p},i} = \bar{c}_\mathrm{p},\ \bar{c}_{\mathrm{v},i} = \bar{c}_\mathrm{v}\ \ \texttt{constant}. \tag{26}$$

The basis for this assumption is that nitrogen is the dominant species in the gas mixture. The implication that the molar specific heats are constant follows from $\bar{c}_{\mathrm{p},i} - \bar{c}_{\mathrm{v},i} = \mathcal{R}$. With this assumption the divergence constraint can be written

$$\begin{aligned}\nabla\cdot\boldsymbol{u} &= \frac{1}{\rho c_\mathrm{p}T}\left(\nabla\cdot(\lambda_\mathrm{LES}\nabla T) + \sum_i c_{\mathrm{p},i}\nabla\cdot\{T(\rho D)_\mathrm{LES}\nabla Y_i\} - \nabla\cdot\dot{\boldsymbol{q}}''_\mathrm{r}\right)\\ &\quad + \frac{1}{\rho}\sum_i\left(\frac{M}{M_i} - \frac{h_i}{c_\mathrm{p}T}\right)\dot{m}'''_i,\end{aligned} \tag{27}$$

where the relation

$$c_{\mathrm{p},i} = \frac{\mathcal{R}}{M_i}\frac{\gamma}{\gamma-1} = \texttt{constant}, \quad c_\mathrm{p} = \sum_i Y_i c_{\mathrm{p},i} = \frac{\mathcal{R}}{M}\frac{\gamma}{\gamma-1} \quad \Rightarrow\ \frac{M}{M_i} = \frac{c_{\mathrm{p},i}}{c_\mathrm{p}} \tag{28}$$

is used to combine the two diffusion terms in Eq. (25). Note that the specific heats are independent of temperature but do depend on the molecular weight of the gas species.

In each form of the divergence constraint the mass consumption terms are, using Eqs. (22) and (23),

$$\frac{1}{\rho}\sum_i\left(\frac{M}{M_i} - \frac{h_i}{c_\mathrm{p}T}\right)\dot{m}'''_i = \frac{1}{\rho}\left(\frac{M\sum_i \nu_i}{\nu_\mathrm{F}M_\mathrm{F}} - \frac{\Delta h_\mathrm{c}}{c_\mathrm{p}T}\right)\dot{m}'''_\mathrm{F} = \frac{M\sum_i \nu_i}{\rho\nu_\mathrm{F}M_\mathrm{F}}\dot{m}'''_\mathrm{F} + \frac{1}{\rho c_\mathrm{p}T}\dot{Q}'''_\mathrm{c}, \tag{29}$$

where $\dot{Q}'''_\mathrm{c}$ is the chemical heat release per unit volume given in Eq. (23). An order of magnitude analysis shows that the first term on the right-hand-side can be neglected for the complex hydrocarbon fuel gases and is not included in the numerical implementation of WFDS. To determine the

the chemical heat release rate per unit volume, Eq. (23), the combustion process must be modeled. This model provides the fuel mass consumption term $\dot{m}'''_{\rm F}$ and is discussed next.

A.1.2 Mixture fraction based combustion model

Even when available, models of detailed chemical kinetics are too computationally expensive to implement in simulations of the scale we are interested in. Instead, we adopt the commonly used mixture fraction based fast chemistry or flame sheet model (Bilger 1980). In this model it is assumed that the time scale of chemical reactions is much shorter than that of mixing (i.e., "mixed is burnt"). The mixture fraction, Z, is defined as:

$$Z \equiv \frac{r_{\rm O_2} Y_{\rm F} - (Y_{\rm O_2} - Y_{\rm O_2}^{\infty})}{r_{\rm O_2} Y_{\rm F}^{\infty} + Y_{\rm O_2}^{\infty}}, \quad 0 \le Z \le 1, \tag{30}$$

where the dependence of $Y_{\rm F}$ and $Y_{\rm O_2}$ on Z can be easily determined by applying the flame sheet assumption, $Y_{\rm F} Y_{\rm O_2} = 0$. Here $Y_{\rm F}^{\infty}$ is the fuel mass fraction in the fuel stream, $Y_{\rm O_2}^{\infty}$ is the oxygen mass fraction in the ambient atmosphere, and $r_{\rm O_2}$ is defined in Eq. (22). If the fuel and oxygen are in stoichiometric proportions, $r_{\rm O_2} Y_{\rm F} = Y_{\rm O_2}$, and they are each completely consumed by the chemical reaction where

$$Z = Z_{\rm st} = Y_{\rm O_2}^{\infty} / (r_{\rm O_2} Y_{\rm F}^{\infty} + Y_{\rm O_2}^{\infty}) \tag{31}$$

is the location of the flame sheet or combustion zone.

With this combustion model the chemical reaction occurs solely as the result of fuel and oxygen mixing in stoichiometric proportion and so is independent of temperature. In reality chemical reactions are dependent on temperature. However, the computational grids used here are much too coarse ($\mathcal{O}$(1 m)) to resolve the combustion zone ($\mathcal{O}$(1 mm)). Thus, in a WFDS simulation the heat released by the combustion process is deposited in computational grid cell volumes that are much larger than volumes occupied by actual combustion zones. For this reason flame temperatures can not be reached and Arrhenius type reaction models that require a resolved temperature field can not be directly used. An alternative is presented below.

The conservation equation for Z is obtained by combining the conservation equations for $Y_{\rm F}$ and $Y_{\rm O_2}$ according to Eq. (30) and using Eq. (22):

$$\frac{\partial \rho Z}{\partial t} + \boldsymbol{u} \cdot \nabla (\rho Z) = -\rho Z \nabla \cdot \boldsymbol{u} + \nabla \cdot \{(\rho D)_{\rm LES} \nabla Z\}. \tag{32}$$

With this equation, Eq. (22), and zero boundary conditions (at $Z = 0, 1$) the dependence of $Y_{\rm CO_2}$ and $Y_{\rm H_2O}$ on Z can be determined. The divergence constraint is

$$\nabla \cdot \boldsymbol{u} = \frac{1}{\rho c_{\rm p} T} \left(\nabla \cdot (\lambda_{\rm LES} \nabla T) - \sum_i Y_i' c_{{\rm p},i} \nabla \cdot (T \rho D \nabla Z) - \nabla \cdot \dot{\boldsymbol{q}}''_{\rm r} + \dot{Q}'''_{\rm c} \right), \tag{33}$$

where Eq. (23) is used for $\dot{Q}'''_{\rm c}$. In the context of the mixture fraction combustion model, the fuel mass consumption term is

$$\dot{m}'''_{\rm F} = Y_{\rm F}' \nabla \cdot (\rho D \nabla Z) - \nabla \cdot (Y_{\rm F}' \rho D \nabla Z) = -Y_{\rm F}'' \rho D |\nabla Z|^2. \tag{34}$$

The numerical implementation of this expression is problematic because $Y_{\rm F}' = dY_{\rm F}/dZ$ is discontinuous. Instead an expression for the mass consumption per unit area of flame sheet, which can

be derived via a line integral through the flame sheet, is used. For example, for oxygen

$$\dot{m}''_{\mathrm{O}_2} = -Y'_{\mathrm{O}_2}|^{Z\le Z_{st}}(\rho D|\nabla Z|)|^{Z=Z_{\mathrm{st}}} = \frac{(\nu M)_{O_2}}{(\nu M)_{\mathrm{F}}}\dot{m}''_{\mathrm{F}}, \tag{35}$$

which implies, using Eq. (23), that the local chemical heat release per unit area of flame sheet is

$$\dot{Q}''_{\mathrm{c}} = -\Delta h_{\mathrm{c}}\frac{(\nu M)_{\mathrm{F}}}{(\nu M)_{O_2}}Y'_{\mathrm{O}}|^{Z\le Z_{st}}(\rho D|\nabla Z|)|^{Z=Z_{\mathrm{st}}}. \tag{36}$$

This expression is used to determine $\dot{Q}'''_{\mathrm{c}}$ at locations corresponding to the flame sheet. The value of the heat of combustion per kg of gaseous fuel is $\Delta h_{\mathrm{c}} = 15600$ kJ kg^{-1}. This is a representative value for a range of grasses reported in Hough (1969) and Susott (1982).

It can be shown that the summation of Eq. (36) along the flame sheet is consistent with the total heat released by the complete combustion of the fuel gas generated by pyrolysis (i.e., arising from the fuel bed) (McGrattan 2005). This very important constraint ensures that the convective and radiative heat transported to the vegetative fuel and to surrounding soot laden gases are consistently coupled to the pyrolysis of the solid fuel. The assumption of complete consumption of the fuel gases is valid only if a sufficient amount of oxygen is present in the volume surrounding the fire. For fire plumes in unbounded domains this is a reasonable assumption. Similar considerations are required for radiative emission as discussed below.

A.1.3 Thermal radiation transport

The radiation transport equation (RTE) for an absorbing-emitting, non-scattering gas is

$$\hat{\boldsymbol{s}}\cdot\nabla I_\lambda(\boldsymbol{x},\hat{\boldsymbol{s}}) = \kappa_\lambda(\boldsymbol{x})[I_{\mathrm{b},\lambda}(\boldsymbol{x}) - I_\lambda(\boldsymbol{x},\hat{\boldsymbol{s}})]. \tag{37}$$

Note that the dependence of the intensity, I, on the frequency of the radiation, λ, is due to the spectral (frequency) dependence of the absorption coefficient κ_λ. However, fires from vegetative fuels are heavily soot laden. Since the radiation spectrum of soot is continuous, it is assumed that the gas behaves as a spectrally independent or gray medium. This results in a significant reduction in computational expense. The spectral dependence is therefore combined into one absorption coefficient, κ, and the emission term is given by the blackbody radiation intensity

$$I_{\mathrm{b}}(\boldsymbol{x}) = \sigma T^4(\boldsymbol{x})/\pi. \tag{38}$$

A table containing the values of κ as function of mixture fraction and temperature for a given mixture of participating gaseous species (H_2O, CO_2) and soot particulate is computed before the simulation begins. A soot evolution model is not used. Instead, the mass of soot generated locally is an assumed fraction, χ_{s}, of the mass of fuel gas consumed by the combustion process. In the WFDS simulations reported here, $\chi_{\mathrm{s}} = 0.02$ is used. Values of χ_{s} for Douglas fir range from less than 0.01 to 0.025 under flaming conditions (Bankston et al. 1981).

Integrating the spectrally independent form of Eq. (37) over all solid angles gives the equation for conservation of radiant energy,

$$\nabla\cdot\dot{\boldsymbol{q}}''_{\mathrm{r}}(\boldsymbol{x}) = \kappa(\boldsymbol{x})[4\pi I_{\mathrm{b}}(\boldsymbol{x}) - U(\boldsymbol{x})], \tag{39}$$

where U is the integrated radiation intensity. This equation states that the net radiant energy lost in a unit volume per unit time is the difference between the emitted and absorbed radiant energy.

The divergence of the radiation flux in Eq. (39) is required in the energy equation, Eq. (18), and in the divergence of the velocity, which is used in the numerical solution procedure, Eq. (33).

As was discussed above, the spatial resolution in the large scale WFDS simulations conducted here is insufficient to resolve the combustion zone. As a result, local gas temperatures on the computational grid in the flame zone region are significantly lower than actual flame temperatures. This requires special treatment of the radiation emission term κI_b in the flame region since it depends on the fourth power of the local temperature. In regions where the temperature is lower and spatial gradients are not so under predicted, the numerical temperatures are more realistic. For this reason the emission term is modeled as

$$\kappa I_\mathrm{b} = \begin{cases} \kappa\sigma T^4/\pi, & \text{outside the flame zone} \\ \chi_\mathrm{r}\dot{Q}'''_\mathrm{c}, & \text{inside the flame zone} \end{cases} \tag{40}$$

where χ_r is the fraction of the chemical heat release rate per unit volume that is radiated to the local volume surrounding the flame region. Note that some of this radiation will be absorbed by the surrounding soot. As a result, for the fire as a whole, the fraction of chemical heat release radiated to a location outside the smoke plume will be smaller than the local value. For hydrocarbon pool fires the local value is $\chi_\mathrm{r} \cong 0.30$ to 0.35 while the global value is less, 0.10 (Koseki and Mulhooand 1991). In wood cribs $\chi_\mathrm{r} \cong 0.20$ to 0.40 (Quintiere 1997). The value used in the simulations is $\chi_\mathrm{r} = 0.35$.

An earlier implementation of the simulation code used the P1 approximation form of the RTE (Baum and Mell 1998). The P1 approximation was also used by Porterie et al. (1998) in the first stages of their two–dimensional model for fire spread through a pine needle bed and by Grishin (1996). The P1 approximation is accurate only when the absorption coefficient of the gases is sufficiently large. Since radiation transport through air, which is optically thin, to the vegetative fuel is an important contribution to the net heat flux on the vegetation ahead of the fire, the P1 approximation is not appropriate in general. For this reason a finite volume method based on that of Raithby and Chui (1990) is used to solve the gray gas form of Eq. (37). It requires approximately 20% of the total CPU time. The spatial discretization of the RTE is the same as that used in the other gas phase conservation equations. The details of the implementation of this approach, including boundary conditions for open and solid boundaries, are in McGrattan (2005).

The set of gas phase conservation equations solved in the simulation consists of the conservation of total mass Eq. (8), the momentum Eq. (9), the mixture fraction Eq. (32), the divergence of the velocity Eq. (33), and the gray gas form of Eq. (37). The equation of state, Eq. (17), is used to obtain the temperature field. In addition, an equation for the pressure field, obtained by taking the divergence of the momentum equation, is solved using a fast direct solver.

A.2 Approach for modeling the solid fuel

The decomposition of a vegetative fuel subjected to a sufficiently high heat flux is a complex process occurring through two general steps: evaporation of moisture and then pyrolysis of the solid. During pyrolysis, chemical decomposition occurs forming char and volatiles that pass out of the solid fuel into the surrounding gas. The above processes are all endothermic. The exothermic process of char oxidation can occur if oxygen is present at a sufficiently hot char surface. If the combustible pyrolysis volatiles mix with enough ambient oxygen at high enough temperatures, then flame ignition occurs. As discussed in the previous section, the combustion model used here assumes that ignition occurs when fuel gas and oxygen mix in stoichiometric proportion, independent of the gas temperature.

Many models of the thermal and mass transport and the kinetics of chemical decomposition for

wood subjected to a prescribed heat flux have been developed. Mostly these models are thermally thick and vary according to how they approximate the anisotropy of the wood material, moisture content, wood constituents, physics of heat and mass transport, and the chemical kinetics of pyrolysis and char oxidation. Reviews of these models can be found in Di Blasi (1993) and Atreya (1983). More recently three–dimensional models have been used (e.g., Yuen et al. (1997)). Numerous thermally thin models for the pyrolysis of cellulose and subsequent flame spread also exist (e.g., Mell et al. (2000); Porterie et al. (2000)).

In all of the above studies either the external heat flux was prescribed or the flame was simulated on a sufficiently fine computational grid that the flame's temperature/structure was well resolved. In the modeling approach taken here the grassland fuel bed is assumed to be comprised of uniformly distributed, non-scattering, perfectly absorbing, thermally thin fuel particles of density $\rho_{\rm s}$ and surface-to-volume ratio $\sigma_{\rm s}$. The thermally thin assumption is commonly used in fire models involving fine wildland fuels (grass and foliage of shrubs and trees) (Rothermel 1972). Note that an emissivity of 0.9 is characteristic of wildland vegetation (Jarvis et al. 1976) so the assumption that a fuel element is a perfect absorber is a reasonable one. The bulk density of the fuel bed is $\rho_{\rm sb}$ and the fraction of the fuel bed volume occupied by the fuel particles, or packing ratio, is $\beta = \rho_{\rm sb}/\rho_{\rm s}$. The temperature evolution equation of the solid fuel in a vegetative fuel bed with these properties is (following Morvan and Dupuy (2004))

$$\beta_{\rm s}\rho_{\rm s}c_{\rm p,s}\frac{\partial}{\partial t}T_{\rm s}(x,y,z,t) = -\nabla\cdot\dot{\boldsymbol{q}}''_{\rm sr} - \nabla\cdot\dot{\boldsymbol{q}}''_{\rm sc} - \dot{Q}'''_{\rm s,vap} - \dot{Q}'''_{\rm s,kin}. \tag{41}$$

Here $\nabla\cdot\dot{\boldsymbol{q}}''_{\rm sr}$ and $\nabla\cdot\dot{\boldsymbol{q}}''_{\rm sc}$ are the divergences of the thermal radiation (spectrally integrated) and conductive heat fluxes on the solid fuel elements within the bulk vegetative fuel bed; $\dot{Q}'''_{\rm s,vap}$ contains the endothermic effect of vaporization of moisture; $\dot{Q}'''_{\rm s,kin}$ contains the contribution of heats (endothermic and exothermic) associated with the thermal degradation of the solid (e.g., pyrolysis, char oxidation); $c_{\rm p,s}$ is the specific heat of the fuel particle, which can contain moisture. This equation, without $\dot{Q}'''_{\rm s,kin}$, was also used by Albini (1985, 1986).

The radiative heat flux can be found by solving the thermal radiation heat transfer equation, Eq. (37), (or an approximation to it, as is done below) in the fuel bed. This requires the absorption coefficient, $\kappa_{\rm s}$, of the bulk fuel bed which can be related to field measurements of the average surface-to-volume ratio and the packing ratio of the fuel particles (NAS 1961),

$$\kappa_{\rm s} = \frac{1}{4}\beta_{\rm s}\sigma_{\rm s} = \frac{1}{4}\frac{w_{\rm s}\sigma_{\rm s}}{\rho_{\rm s}h_{\rm s}}, \tag{42}$$

where $w_{\rm s}$ is the fuel bed loading and $h_{\rm s}$ is the fuel bed height. This expression for the absorption coefficient has been used in other fire spread models (Albini 1985, 1986; De Mestre et al. 1989; Morvan and Dupuy 2001, 2004) and has been experimentally validated for vegetative fuels (Butler 1993).

The bulk conductive heat flux term in Eq.(41) is approximated by the volume-averaged sum of the local flux on the surface of individual fuel particles. For a representative volume V containing $N_{\rm p}$ fuel particles

$$\nabla\cdot\dot{\boldsymbol{q}}''_{\rm sc} \cong \frac{\sum_{i=1}^{N}\int\dot{\boldsymbol{q}}''_{\rm sc,p}\cdot\hat{\rm n}\;dS_{{\rm p},i}}{V} \cong \frac{\dot{q}''_{\rm sc,p}N_{\rm p}S_{\rm p}}{V} = \frac{N_{\rm p}S_{\rm p}}{N_{\rm p}V_{\rm p}}\frac{N_{\rm p}V_{\rm p}}{V}\;\dot{q}''_{\rm sc,p} = \sigma_{\rm s}\beta_{\rm s}\;\dot{q}''_{\rm sc,p}, \tag{43}$$

where $S_{\rm p}$, $V_{\rm p}$ and $\dot{q}''_{\rm sc,p}$ are the surface area, volume, and net surface conductive heat flux associated with a representative fuel particle, respectively. The conductive heat flux is assumed to be uniform

across the surface of the fuel particle which is consistent with the assumption that the particle is thermally thin and surrounded by gas of constant temperature $T_{\rm g}$.

Model Eqs. (41), (42) and (43) have been used to predict heat transfer in two-dimensional vegetative fuel beds by Albini (1986) to obtain steady-state fire spread rates ($\dot{Q}'''_{\rm s,kin} \equiv 0$). These equations along with a model for thermal degradation (to determine $\dot{Q}'''_{\rm s,kin}$) have also been used in the two-dimensional simulation of Morvan and Dupuy (2004) (and their earlier work). Morvan and Dupuy solve the governing equations for the solid fuel and gas phase on the same computational grid with a cell size of 10 mm in the pyrolysis zone. This is not possible in the present study since the gas phase cells are $\mathcal{O}(1)$ m. Instead, the fuel bed is given its own uniform computational grid on which Eq. (41) is solved (see Fig. 20). Within the gas phase computational grid the fuel bed is present as a momentum drag only. Thermal and mass flux interaction of the gas and vegetative grids occurs at the gas/vegetation boundary, $(x_\Gamma, y_\Gamma, 0)$ in gas phase coordinates. The temperature of the solid fuel in the vegetative fuel bed is assumed to depend on the vertical coordinate only, $T_{\rm s}(x_{\rm s}, y_{\rm s}, z_{\rm s}, t) = T_{\rm s}(x_\Gamma, y_\Gamma, z_{\rm s}, t)$ beneath each gas phase grid cell along the gas/vegetation boundary. The resolution of the grid used for the vegetation is $\Delta z_{\rm s} \leq (3\kappa_{\rm s})^{-1}$, is based on the optical depth of the fuel bed, ${\kappa_{\rm s}}^{-1}$ (Morvan and Dupuy 2001). Initially, the number of layers spanning the height of the fuel bed is $N_{\rm L} = h_{\rm s}{\Delta z_{\rm s}}^{-1}$. The grassland fuel bed is assumed to burn from the top down causing the total number of layers to decrease with time. It should be noted that this assumption of top down burning is more consistent with field observations of head fires, which spread with the ambient wind, as opposed to fire spread either into the wind (backing fire) or across the ambient wind (flanking fire). As the fuel bed burns away, the term in the square brackets in Eq. (12) decreases in magnitude (i.e., the influence of drag decreases).

It is assumed that radiation within the fuel bed is spectrally independent and travels in only two directions, either downward or upward. This is commonly called the forward-reverse radiation transfer model (Ozisk 1973; Mell and Lawson 2000). The net radiative flux within the fuel bed has contributions from the downward radiative flux due to the fire, incident on the top of fuel bed ($\dot{q}''^{,-}_{\rm sr,i}$, see Fig. 20) and from the radiative flux due to local self emission (integrals in Eq. (44) below). With these assumptions the net radiative flux at a nondimensional distance $\eta_{\rm s} = \kappa_{\rm s} z_{\rm s}$ from the top of the fuel bed is:

$$\begin{aligned}
\dot{\boldsymbol{q}}''_{\rm sr}(\eta_{\rm s}) &= \dot{\boldsymbol{q}}''^{+}_{\rm r} + \dot{\boldsymbol{q}}''^{-}_{\rm r} \\
&= \dot{q}''^{+}_{\rm sr,i} \exp(-[\eta_{\rm s,h} - \eta_{\rm s}]) + \sigma \int_{\eta_{\rm s}}^{\eta_{\rm s,h}} T_{\rm s}^4 \ \exp(-[\eta'_{\rm s} - \eta_{\rm s}]) d\eta'_{\rm s} \\
&\quad -\dot{q}''^{-}_{\rm sr,i} \exp(-\eta_{\rm s}) - \sigma \int_0^{\eta_{\rm s}} T_{\rm s}^4 \ \exp(-[\eta_{\rm s} - \eta'_{\rm s}]) d\eta'_{\rm s}, \qquad (44)
\end{aligned}$$

where $\eta_{{\rm s},h} = \kappa_{\rm s} h_{\rm s}$. The net radiative flux on the bottom boundary of the fuel bed is assumed to be zero (this defines $\dot{q}''^{+}_{\rm sr,i}$). This radiation boundary assumption was also made by Albini (1986) for fire spread through surface fuels where the bottom boundary is soil. The radiation transfer computation in the gas phase provides $\dot{q}''^{-}_{\rm sr,i}$.

With the above assumptions, integrating Eq. (41) over a control volume $dx_\Gamma dy_\Gamma dz_{\rm s}$ centered at $z_{{\rm s},n}$, the center of the nth cell in the solid fuel's computational grid (see Fig. 20 below), gives

$$\begin{aligned}
[m''_{\rm s} c_{\rm p,s} \frac{\partial T_{\rm s}}{\partial t}]_n &= -[\dot{\boldsymbol{q}}''_{\rm sr}(\eta_{\rm s}^+) \cdot \hat{\boldsymbol{n}}^+ + \dot{\boldsymbol{q}}''_{\rm sr}(\eta_{\rm s}^-) \cdot \hat{\boldsymbol{n}}^-]_n - [\sigma_{\rm s}\beta_{\rm s} \ \dot{q}''_{\rm sc,p} + \dot{Q}'''_{\rm s,vap} + \dot{Q}'''_{\rm s,kin}]_n \ \Delta z_s \\
&= [\dot{q}''_{\rm s,net}]_n - [\dot{Q}'''_{\rm s,vap} + \dot{Q}'''_{\rm s,kin}]_n \ \Delta z_s. \qquad (45)
\end{aligned}$$

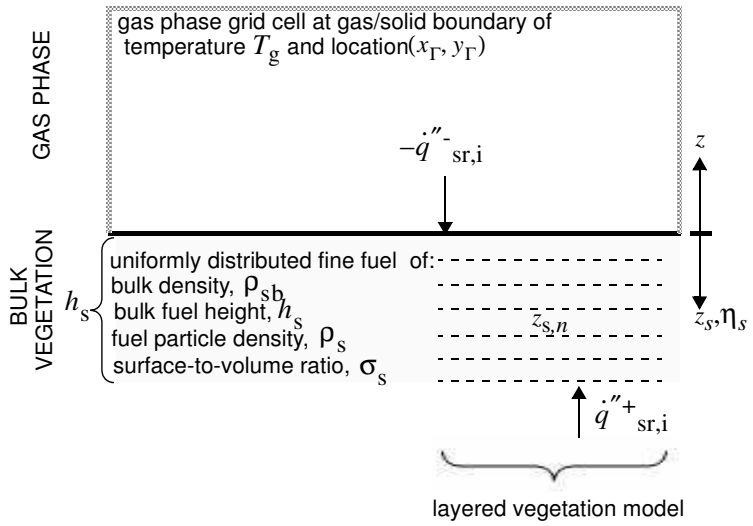

Figure 20: This figure summarizes the solid phase model. The vegetative fuel is characterized by its bulk density, $\rho_{\rm sb}$, the fuel particle density, $\rho_{\rm s}$, the surface-to-volume ratio of the fuel particles, $\sigma_{\rm s}$, and the height of the bulk fuel, $h_{\rm s}$. The fuel bed is divided into $N_{\rm L}$ layers and the evolution equations governing the heat up, drying, and pyrolysis of the vegetative fuel are solved within each layer as described in the text.

Here

$$[\dot{q}''_{\rm s,net}]_n = -\dot{\boldsymbol{q}}''_{\rm sr}(\eta^+_{{\rm s},n}) \cdot \hat{\boldsymbol{n}}^+ - \dot{\boldsymbol{q}}''_{\rm sr}(\eta^-_{{\rm s},n}) \cdot \hat{\boldsymbol{n}}^- - \sigma_{\rm s}\beta_{\rm s}\dot{q}''_{\rm sc,p}\Delta z_{\rm s} = \dot{q}''_{\rm sr,net,}n + \dot{q}''_{\rm sc,net,}n \tag{46}$$

is the net heat flux on the bulk solid fuel; $\eta^-_{{\rm s},n}$ and $\eta^+_{{\rm s},n}$ are the locations of the lower and upper horizontal faces, respectively, of the nth grid cell; and $\hat{\boldsymbol{n}}^+$, $\hat{\boldsymbol{n}}^-$ are the outward facing normals on these faces. All other quantities are cell-centered. It is assumed that the rate at which thermal energy is stored in the control volume, the right-hand-side of Eq. (45), and the heat sinks and sources associated with vaporization and thermal degradation, are constant throughout the cell volume. Values of $\dot{q}''_{\rm sr,net,1}$ and $\dot{q}''_{\rm sc,net,1}$ versus time were plotted previously on Fig. 2. In general, the solid fuel mass per area in grid cell n, $[m''_{\rm s}]_n$, is composed of dry virgin vegetative fuel and moisture $m''_{\rm s} = m''_{\rm s,v} + m''_{\rm s,m}$. Initially $[m''_{\rm s,v}(t=0)]_n = w_{\rm s}\Delta z_{\rm s}/h_{\rm s}$ and $[m''_{\rm s,m}(t=0)]_n = M[m''_{\rm s,v}(t=0)]_n$ where M is the moisture fraction. M is defined to be the mass of initial moisture in a fuel particle divided by its mass when dry. The specific heat of the fuel particle has, in general, contributions from moisture and vegetation (Porterie et al. 1998):

$$c_{\rm p,s} = \frac{m''_{\rm s,v}c_{\rm p,v} + m''_{\rm s,m}c_{\rm p,m}}{m''_{\rm s}}, \tag{47}$$

where $c_{\rm p,v}$ (which depends on $T_{\rm s}$) and $c_{\rm p,m}$ are given in Table 1.

The conductive heat flux on the surface of a fuel particle, $\dot{q}''_{\rm sc,p}$, in Eq. (46) is determined using

a convective heat transfer coefficient, h_c, for a vertical cylinder (Holman 1981), and is defined by

$$\dot{q}''_{sc,p} = h_c(T_s - T_g), \quad h_c = 1.42(|T_s - T_g|/\Delta z_s)^{1/4}. \tag{48}$$

T_g is the temperature in the bottom gas phase grid cell bordering the fuel bed, and Δz_s is the length of the cylinder in the nth fuel layer.

The temperature equation, Eq. (45), for the fuel bed is solved assuming a two stage endothermic decomposition process (water evaporation followed by solid fuel pyrolysis). At this stage in the model development char oxidation is not accounted for, and $\dot{Q}'''_{s,kin} = \dot{Q}'''_{s,pyr}$. In a given fuel layer the virgin fuel dries and then undergoes pyrolysis until the solid mass remaining equals $\chi_{char} w_s / N_L$ where χ_{char} is the char fraction of the solid fuel and N_L equals the original number of layers in the fuel model (see Fig. 20). A char mass fraction of $\chi_{char} = 0.2$ was used based on measurements of grass fuels by Susott (1982).

Moisture is removed in a manner similar to previous models (Albini 1985; De Mestre et al. 1989; Margeri and Sero-Guillaume 2002; Morvan and Dupuy 2004). The temperature of the vegetative fuel bed evolves according to Eq. (45). Once T_s reaches boiling temperature, T_b, it is assumed that drying requires all of the available heat so that $T_s = T_b$ until all the moisture has evaporated. With these assumptions the drying stage of fuel decomposition is modeled as:

$$\begin{aligned}
\dot{Q}'''_{s,vap} &= \dot{m}''_{s,m} \Delta h_{vap} / \Delta z_s, \\
\dot{m}''_{s,m} &= \begin{cases} 0, & T_s < T_b, \\ \dot{q}''_{s,net} / \Delta h_{vap}, & T_s = T_b,\ m''_{s,m} > 0,\ \dot{q}''_{s,net} > 0, \end{cases} \\
\dot{Q}'''_{s,pyr} &= 0.
\end{aligned} \tag{49}$$

After all the moisture is boiled off, the temperature of the fuel bed is free to change according to Eq. (45) with $m''_{s,m} = 0$. With a net influx of heat, T_s continues to rise, eventually reaching a point $T_s = T_{pyr}$, where pyrolysis begins and $\dot{Q}'''_{s,pyr} \neq 0$.

This is as far as the physics-based fire/fuel spread models such as Albini (1985) and De Mestre et al. (1989) go since the incident heat flux from the fire is assumed, allowing the steady-state fire spread rate to be determined based on how long it takes T_s to reach T_{pyr}. In our case, however, the computer simulation supplies the time-dependent heat flux based on the behavior of the simulated fire, which drives the pyrolysis of the solid fuel and determines $\dot{m}''_{s,pyr}$, the rate at which fuel gas is generated. Physics-based computer simulation approaches of fire spread in vegetative fuels that have well resolved gas phase flames, such as Porterie et al. (1998) and Morvan and Dupuy (2001), use temperature dependent Arrhenius kinetics for pyrolysis and char oxidation. More recently Morvan and Dupuy (2004) found that a simple temperature dependent pyrolysis mass loss rate was as accurate as a more complicated Arrhenius expression. The model for solid fuel thermal degradation used here uses the temperature dependent mass loss rate expression in Morvan and Dupuy (2004). This pyrolysis model was based on thermogravimetric analysis of number of vegetation species (Dimitrakipoulos 2001; Moro 1997). Since char oxidation is not modeled the smoldering or glowing combustion in the grass, after the fire front has passed, is not present. Thus, in the simulations reported here the pyrolysis stage of decomposition is (Morvan and Dupuy 2004):

$$\begin{aligned}
\dot{Q}'''_{s,vap} &= 0, \\
\dot{Q}'''_{s,pyr} &= \dot{m}''_{s,pyr} \Delta h_{pyr} / \Delta z_s \\
\dot{m}''_{s,pyr} &= \begin{cases} 0, & T_s < 127 \text{ C}, \\ \left(\dot{q}''_{s,net} / \Delta h_{pyr}\right) (T_s - 127)/100, & 127 \text{ C} \le T_s \le 227 \text{ C},\ \dot{q}''_{s,net}, > 0, \\ & \text{and } m''_s > \chi_{char} w_s. \end{cases}
\end{aligned} \tag{50}$$

The heat of pyrolysis, $\Delta h_{\rm pyr}$, is 416 kJ kg^{-1} (Morvan and Dupuy 2004). When the mass loss, in the $n^{\rm th}$ solid phase cell, is such that $m''_{{\rm s},n} = \chi_{\rm char} w_s / N_{\rm L} = m'''_{{\rm char},n}$ then the fuel in that layer is assumed to be consumed and it is removed from the solid fuel model.

B Nomenclature

Variable	Units	Description
c_{p}	kJ kg^{-1}K^{-1}	specific heat at constant pressure
$c_{\mathrm{p},i}$	kJ kg^{-1}K^{-1}	specific heat of species i at constant pressure
$\bar{c}_{\mathrm{v},i}$	kJ/kmole·K	molar specific heat of species i at constant volume
D	m^2 s^{-1}	mass diffusivity
d	m	depth of head fire
d_{ig}	m	depth of ignition fire-line
$\boldsymbol{g}$	m/s^2	ambient acceleration vector
$\mathcal{H}$	m^2/s^2	modified pressure term in momentum equation
$h = \sum_i Y_i h_i$	kJ/kg	mixture enthalpy
h_{b}	m	height of bulk vegetative fuel
h_i	kJ/kg	specific enthalpy of species i
$\bar{h}_i = h_i M_i$	kJ/kmole	molar specific enthalpy of species i
h_{s}	m	height of solid fuel
$\mathbf{I}$	-	identity matrix
$I_\lambda(\boldsymbol{x}, \hat{\boldsymbol{s}})$	W·MHz/m^2 · sr	spectral radiation intensity
$I_{\mathrm{b}}(\boldsymbol{x}, \hat{\boldsymbol{s}})$	W·MHz/m^2 · sr	blackbody radiation intensity
L_{ig}	m	length of ignition line
m''_{m}	kg m^{-2}	mass loading of moisture in vegetative fuel
m''_{s}	kg m^{-2}	mass loading of moisture in vegetative fuel
$\dot{m}''_{\mathrm{s,pyr}}$	kg/m^2·s	mass flux of fuel gas due to pyrolysis of vegetative solid fuel
$\dot{m}'''_i$	kg/s · m^3	chemical mass consumption of gas species i
$\dot{m}''_{\mathrm{m,e}}$	kg/m^2·s	mass flux of water vapor from vegetative fuel element during drying
M	-	fuel moisture content as fraction of oven dried fuel mass, expressed as a percentage. %
M_i	kg/kmole	molecular weight of gas species i
$M = (\sum_i Y_i/M_i)^{-1}$	kg/kmole	average molecular weight of gas mixture
$\hat{\boldsymbol{n}}$	-	unit normal vector
$\dot{Q}'''_{\mathrm{c}}$	kW/m^3	heat release rate per unit volume due to chemical reactions
p_{d}	Pa	dynamic pressure
p_o	Pa	a thermodynamic pressure
$\mathcal{R} = 8.314$	kJ kmole^{-1}K^{-1}	universal gas constant
R_{o}	m s^{-1}	experimentally observed head fire spread rate
R_{s}	m s^{-1}	empirically derived potential quasi-steady head fire spread rate
$\dot{q}''$	kW m^{-2}	magnitude of heat flux
$\dot{\boldsymbol{q}}''$	kW m^{-2}	heat flux vector
$\hat{\boldsymbol{s}}$	-	unit vector in direction of radiation intensity
T	°C	temperature
$\boldsymbol{u}$	m s^{-1}	velocity vector
w_{s}	kg m^{-2}	vegetative fuel loading
U	W m^{-2}	integrated radiation intensity
U_2	m s^{-1}	wind speed in direction of spread at 2 m above ground
$\boldsymbol{x}$	m	position vector
W	m	width of head fire

$Y_i = \rho_i/\rho$	-	local mass fraction of species i
Y_{F}^{∞}	-	mass fraction of fuel in fuel stream
$Y_{\mathrm{O_2}}^{\infty}$	-	mass fraction of oxygen in oxidant
Z	-	local mixture fraction
Z_{st}	-	stoichiometric value of the mixture fraction
β	-	packing ratio, $\rho_{\mathrm{b}}/\rho_{\mathrm{e}}$
$\gamma_i = c_{\mathrm{p},i}/c_{\mathrm{v},i}$	-	ratio of species i specific heats
$\Delta\bar{h}_{\mathrm{c}}$	kJ/kmole	molar based heat of combustion
$\eta_{\mathrm{s}} = \kappa_{\mathrm{s}} z_{\mathrm{s}}$	-	nondimensional distance from top of fuel bed
Δh_{c}	kJ/kg	mass based heat of combustion
Δh_{vap}	kJ/kg	heat of vaporization of water
Δh_{pyr}	kJ/kg	heat of pyrolysis of vegetative fuel
$\Delta x, \Delta y, \Delta z$	m	length of computational cell in x, y, z directions
σ_{s}	m^{-1}	surface-to-volume ratio of fuel elements
σ	5.67×10^{-11} $\mathrm{kWm^{-2}K^{-4}}$	Stefan-Boltzmann constant
λ	W/m·K	thermal conductivity of the gaseous mixture
μ	kg /m· s	dynamic viscosity of the gaseous mixture
ν_i	-	stoichiometric coefficient of species i
ρ	$\mathrm{kg/m^3}$	total density of gas
ρ_{sb}	$\mathrm{kg/m^3}$	bulk density of solid fuel
ρ_{s}	$\mathrm{kg/m^3}$	fuel particle density
τ	$\mathrm{kg/m \cdot s^2}$	viscous stress tensor
χ_{char}	-	fraction of virgin solid fuel converted to char
χ_{r}	-	fraction of local chemical heat release radiated to surroundings
χ_{s}	-	fraction of consumed fuel mass converted to soot

Subscripts

a	ambient
b	boiling or bulk vegetative fuel quantity
c	convective
i	incident flux on boundary
ig	ignition
i	gaseous species
g	gas phase
m	moisture
net	net quantity
o	outward flux at boundary or observed value
r	radiative
s	solid (vegetative) fuel
v	virgin dry vegetation
F	fuel species
LES	value used in large eddy simulation
O_2	oxygen species
λ	spectral dependence

Superscripts

$\prime$	derivative with respect to mixture fraction, $(\ )' = d(\ )/dZ$
T	transpose

Table 1: Thermophysical properties required in model and values used in base case simulations. Properties that were not measured in the two experimental field studies F19 or C064 are denoted by a hyphen (-). Values of these unknown properties in the simulation were either assumed or representative values were obtained from the literature sources cited.

	symbol, units	value used	F19	C064	other source (if needed)
gas phase	Δh_c, kJ kg^{-1}	15600	-	-	grass (Susott 1982; Hough 1969)[a]
	χ_r	0.35	-	-	wood cribs (Quintiere 1997)[a]
	χ_s	0.02	-	-	Douglas fir (Bankston et al. 1981)[a]
	dT_a/dz, C m^{-1}	0.0	-	-	assumed
	U_2, m s^{-1}	experimental	4.8	4.6	
	$T_{g,a}$, C	experimental	34	32	
solid phase	σ_s, m^{-1}	experimental	12240	9770	
	χ_{char}	0.2	-	-	grass (Susott 1982)[a]
	$c_{p,v}$, kJ kg^{-1}C^{-1}	varies with T_s	-	-	= 1.11 + 0.0037 T_s (Parker 1988)
	$c_{p,m}$, kJ kg^{-1}C^{-1}	4.22	-	-	Incropera and Dewitt (1996)
	h_s, m	experimental	0.51	0.21	
	ρ_s, kg m^{-3}	512	-	-	grass (Rothermel 1972)
	w_s, kg m^{-2}	experimental	0.313	0.283	
	β_s	experimental	0.0012	0.0026	
	M %	experimental	5.8	6.3	
	ΔH_p kJ kg^{-1}	416	-	-	see discussion in Sec. A.2
	$T_{s,a}$, C	$T_{g,a}$	-	-	assumed

[a]representative value from range of values found in the cited reference

Table 2: Simulation parameters for production runs. The horizontal grid cell sizes are equal $\Delta x = \Delta y$. The values of Δx given in the Table are for a 300 m $\times$ 300 m region in the center of the overall simulation domain. Outside this central region the horizontal grid cells are twice this size. The vertical grid size increases upward (72 grid cells are used). Each simulation required sixteen million grid cells and 11 (1.8 GHz) processors. Case F19 required 44 cpu hours for 100 s of simulated time. Case C064 required 25 cpu hours for 100 s of simulated time. Case C064 required less resources because the overall heat release rate was approximately half that of case F19, resulting in smaller buoyancy induced velocities and, therefore, larger time steps.

simulation	u_2, m s^{-1}	$L_{\rm ig}$,m ———- $d_{\rm ig}$, m	fuel bed	grass plot x, y extent, m, m	sim. domain extent, km ———- Δx; Δz, m
head spread	1, 3, 4, 5	8, 25, 50, 100 ———- 6.7,6.7,3.3,3.3	= exp F19	200 $\times$ 200	1.5 $\times$ 1.5 $\times$ 0.2 ———- 1.6; 1.4 $\rightarrow$ 5.5
exp F19	4.9	175 ———- 3.3	see Table 1	200 $\times$ 200	1.5 $\times$ 1.5 $\times$ 0.2 ———- 1.6; 1.4 $\rightarrow$ 5.5
exp C064	4.6	50 ———- 1.6	see Table 1	104 $\times$ 108	1.5 $\times$ 1.5 $\times$ 0.08 ———- 1.6; 0.6 $\rightarrow$ 5.5